Progress in Aerospace Sciences 151 (2024) 101044

Contents lists available at ScienceDirect

Progress in Aerospace Sciences

journal homepage: www.elsevier.com/locate/paerosci

Retro-propulsion in rocket systems: Recent advancements and challenges for the prediction of aerodynamic characteristics and thermal loads

Tamas Bykerk *, Sebastian Karl, Mariasole Laureti, Moritz Ertl, Tobias Ecker

DLR Goettingen, Bunsenstr. 10, 37073, Germany

ARTICLE INFO

Keywords:
Retro-propulsion
Re-usable launchers
CFD
Wind tunnel testing

ABSTRACT

This paper presents a review of recent literature on the application of retro-propulsion in earth based rocket systems, with a specific focus on the recent advancements and challenges associated with the prediction of aerothermal and aerodynamic characteristics of re-usable boosters. It gives an overview of current system architectures and mission profiles, while discussing the trends in future vehicle design. The effects of various flight conditions on thermal loads and vehicle aerodynamics are discussed, with particular attention given to the interactions between plume and vehicle, as well as the interplay between individual nozzle exhausts. A short evaluation of wind tunnel testing capabilities and scaling challenges is given, before the use of computational fluid dynamics for retro-propulsion applications is discussed. Finally, a summary is given, which emphasises future needs surrounding the accurate prediction of the vehicle aerothermal and aerodynamic characteristics.

Contents

* Corresponding author.
E-mail address: tamas.bykerk@dlr.de (T. Bykerk).

https://doi.org/10.1016/j.paerosci.2024.101044
Received 30 June 2024; Received in revised form 9 September 2024; Accepted 10 September 2024

Acronyms

AoA	Angle of Attack
CFD	Computational Fluid Dynamics
LES	Large Eddy Simulation
RANS	Reynolds Averaged Navier-Stokes
FV	Finite Volume
CPU	Central Processing Unit
BN	Bleed Nozzle
ESA	European Space Agency
SST	Shear Stress Transport
RSM	Reynolds Stress Model
FLPP	Future Launchers Preparatory Programme
NOx	Oxides of Nitrogen
SSTO	Single Stage to Orbit
TSTO	Two Stage to Orbit
RETALT	RETro propulsion Assisted Landing Technologies
DLR	German Aerospace Center
EU	European Union
JAXA	Japanese Aerospace Exploration Agency
CNES	French National Center for Space Studies
SALTO	reuSable strAtegic space Launcher Technologies and Operations
ATDB	Aero-thermal Database
VTVL	Vertical Take-Off Vertical Landing
RTLS	Return to Launch Site
DRL	Downrange Landing
CoG	Center of Gravity
EPR	Exit Pressure Ratio
TVC	Thrust Vector Control
AoR	Angle of Roll
MFR	Momentum Flux Ratio
APR	Ambient Pressure Ratio
TER	Total Enthalpy Ratio
O/F	Oxidiser to Fuel Ratio
VMK	Vertical Test Section
DSMC	Direct Simulation Monte-Carlo
URANS	Unsteady Reynolds Averaged Navier-Stokes
DES	Detached Eddy Simulation
SA	Spalart Allmaras
NO	Nitric Oxide

Abbreviations

D_{NE}	Nozzle exit diameter
T_w	Wall Temperature
u	Freestream x-velocity
M	Mach number
q_∞	Dynamic pressure
A_B	Base area
q	Convective heat flux
T	Thrust
ρ	Density
P	Pressure
C_p	Specific heat capacity
γ	Ratio of specific heats
Re	Reynolds Number
T_T	Total Temperature
P_e	Exit pressure
P_a	Ambient pressure

Subscripts

∞	Freestream condition
j	Jet

1. Introduction

Retro-propulsion is a technique which involves the firing of rocket engines opposite to the direction of travel and has emerged as a transformative technology in the design and operation of reusable launch systems. Traditionally associated with spacecraft descent and landing on celestial bodies [1], retro-propulsion has found renewed interest and expanded applications in the realm of re-usable launch vehicles for earth orbit missions [2]. One of the notable implementations of retro-propulsion is the controlled descent of the first stage of a rocket. After propelling the payload to a certain altitude, the first stage initiates a controlled descent back to Earth. Retro-propulsion engines are activated to counteract the vehicle's forward momentum and shield critical components from the harsh conditions of re-entry, allowing for a precise and targeted return to the landing site or recovery platform. SpaceX's Falcon 9 stands as a prominent example of the practical implementation of retro-propulsion in reusable launch systems (see Fig. 1).

While the application of retro-propulsion for re-usable, orbital class boosters is new, the investigation into the behaviour of a jet with a counterflow has been in the literature since the 1950s. Early examples include wind tunnel campaigns to evaluate the influence of a forward facing jet on aerodynamic coefficients and boundary layer transition for axisymmetric bodies of revolution [3]. This was followed by several studies in the 1960s and 1970s investigating the impact of supersonic retro-propulsion and stagnation point flow injection on the augmentation of heating and shock system topology [4–6]. Here key observations were made including the dependence of plume shape and shock structures on various parameters including the ratio of nozzle exit pressure to freestream static pressure, as well as the conditions in the reservoir feeding the plume. Various model geometries were tested experimentally, including cylindrical [7] and conical [8–10] bodies of revolution which still have a high relevance to this day. Analytical techniques also emerged as part of these works to predict the variation in shock stand-off distance. Experimental campaigns focused on supersonic jets with subsonic counterflows, which are related to conditions prior to landing, were also investigated during this time period [11].

Practical applications of retro-propulsion have spanned the entire history of manned spaceflight. Early examples include retro-packs attached to the Vostok and Mercury capsules in the 1950s, with better

Fig. 1. Falcon 9 landing (SpaceX Photos, CC0, via Wikimedia Commons).

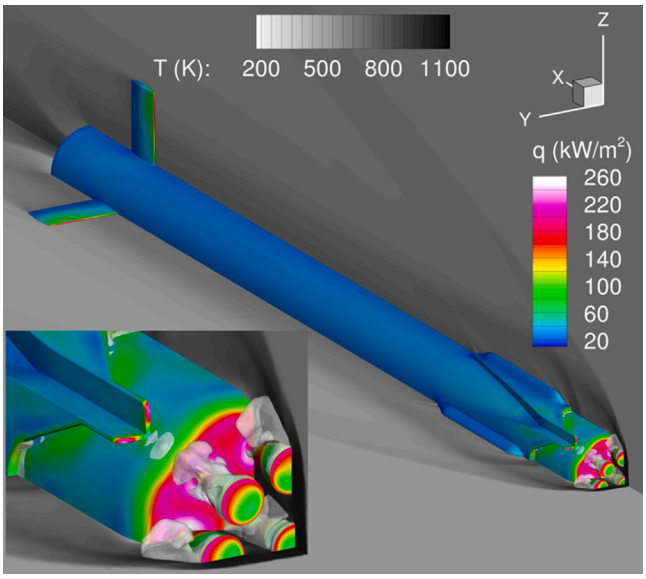

Fig. 2. RETALT TSTO configuration during aerodynamic glide phase at Mach 4.3 and 23km altitude [39].

integrated retro-rocket systems emerging during the 1960–80s with the Gemini, Soyuz and finally, the Space Shuttle programs. These retro-systems were critical for mission success as they enabled a de-orbit manoeuvre to take place before the vehicles velocity was slowed through aerodynamic drag and parachute deployment. The Soyuz capsule also uses retro-rockets in the final seconds of flight, where a short burn moments before impact is initiated to decrease the velocity of the capsule when it lands in the Baikonour desert. For spacecraft landing on celestial or planetary bodies without atmospheres, retro-propulsion through the entire descent phase is necessary. This was exhibited during the Apollo missions, where lunar landings were achieved by firing the main engine opposite to the direction of travel to regulate forward and vertical velocity, ultimately culminating in many successful missions. Martian landings pose the problem of enough atmospheric density to create significant vehicle heating, but not allow a sufficiently low terminal descent velocity. As a result, past strategies have used a combination of traditional blunt body re-entry approaches with air bags, parachutes and retro-propulsion. However, as the future of space exploration looks towards landing higher mass payloads with greater accuracy, new concepts deviating from Viking era technology need to be developed [12]. Recent advancements in vehicle design are evaluating both capsule and lifting body concepts which remove the need for parachutes by employing a longer powered descent after re-entry. This can be achieved with retro-propulsion systems integrated on the underside of the vehicles along with retractable landing legs which deploy before landing [13]. These concepts are currently undergoing numerical and experimental evaluations to determine feasibility and the merits of each design [14–16], as well as understand the complex aerodynamics and underbody heating which can arise when firing the engines into a high dynamic pressure supersonic counter flow. While the applications of retro-propulsion associated with interplanetary travel are not specifically relevant to this paper, which will discuss challenges and advancements from the perspective of earth applications, it is still important to recognise this work. Overlaps in Mach and dynamic pressure ranges, as well as numerical and experimental approaches which are relevant to both earth and martian flights have been shown to exist [17], meaning both communities can mutually benefit from knowledge gained.

These historical advancements in retro-propulsion set the stage for Falcon 9's groundbreaking achievement in December 2015, proving the feasibility of the vertical take-off vertical landing (VTVL) concept. The lack of belief in the SpaceX approach is clearly visible in the literature, which in the years preceeding 2015 typically focused on horizontally landing boosters or glide vehicles [18–21]. From 2016 onwards, analyses of Falcon 9 flights began to emerge to understand the technological challenges that SpaceX had overcome to have a working VTVL first stage. The bulk of this literature stemmed from Europe, with projects such as ENTRAIN (European Next Reusable Ariane), which were groundwork studies to form the basis for future knowledge in the VTVL space [22,23]. From an aerodynamics and heat loading perspective, computational fluid dynamics (CFD) simulations including Reynolds Averaged Navier–Stokes (RANS) and Large Eddy Simulation (LES) approaches were completed, which provided a basis for grasping the ability of RANS to effectively produce a good representation of an inherently unsteady flow field [24]. This paved the way for follow up studies with increasing levels of complexity. The RETALT project (RETro propulsion Assisted Landing Technologies), funded within the European Union (EU) Horizon 2020 framework, investigated both a single stage to orbit (SSTO) and two stage to orbit (TSTO) configuration (see Fig. 2). Within this project, a comprehensive set of wind tunnel tests and numerical computations were conducted to characterise the vehicle aerodynamics and aerothermodynamics through a wide range of flight conditions [25–37], including both forward and backward flight. One of the main contributions of this project to the body of knowledge is the comprehensive aerodynamic database, containing both numerical and experimental results, which has been made available to the public [38].

This was followed by the RETPRO project, which completed a similar wind tunnel test campaign, but had a stronger focus on numerical rebuilding of the wind tunnel tests and extrapolation to flight [40–45]. The activities were carried out under a programme of and funded by the European Space Agency (ESA) – through the Future Launchers Preparatory Programme (FLPP). As part of both RETALT and RETPRO, unique experiments were conducted, including landing burn tests with a reacting H2/O2 exhaust plume [46]. Running concurrently to these scientific studies, the development of flight demonstrators has also taken place. While not all programs are focused on aerodynamics and aerothermodynamics, such as the Frog project [47], each have a specific aim to increase the technology readiness level, with the

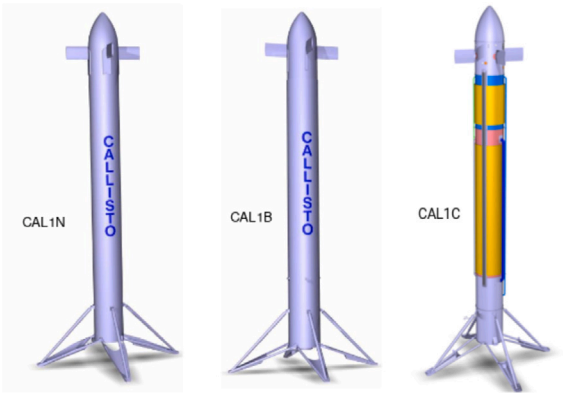

Fig. 3. Illustration of various iterations of the Callisto test bed highlighting increased complexity of the external geometry [65].

final goal of achieving a re-usable launch system in Europe. Callisto (Cooperative Action Leading to Launcher Innovation in Stage Tossback Operations) is one of these projects. Callisto is a collaboration between the German Aerospace Center (DLR), the French National Center for Space Studies (CNES) and the Japan Aerospace Exploration Agency (JAXA) which aims at demonstrating all relevant technologies needed for a retro-propulsion booster and is scheduled to fly in 2026 from Kourou. Aerodynamic characterisation of the vehicle both with and without plume have been conducted since 2018 [48–64]. The publications generated during this project are significant and effectively document the transition from a configuration more representative of what typically appears in research projects to a realistic flight vehicle. This can be seen through the increasing complexity of the outer mold line which has been investigated experimentally and numerically, where external pipes, slits and channels are modelled (see Fig. 3). This bridges some knowledge gaps surrounding the influence of these features on aerodynamic drag during backward flying phases of flight, as well as areas which are susceptible to high heating during retro-burns. These findings are possible thanks to the extensive aerodynamic and aerothermal databases which have been continuously generated for an increasing selection of parameters during all project phases. The aerodynamic and aerothermal loads estimations are used as input on system and product level, for example, for the design of guidance, control and landing systems.

Upcoming vehicles within Europe include Themis, an ESA reusable rocket stage demonstrator conceived as an integral part of the ESA's FLPP [66]. The EU is also contributing to increase the maturity level of Themis through the Horizon Europe project SALTO (reuSable strAtegic space Launcher Technologies & Operations). This project aims to enhance reusable technologies by developing hardware that can withstand multiple launches and landings, reducing the cost per launch, and by creating efficient processes for the rapid turnaround of launch vehicles [67]. The Themis programme will serve as a key technological building block for the next generation of European reusable launchers, i.e. Ariane Next and Ariane Ultimate. The development of these larger, more capable rocket systems will most likely result in a reduction of the literature output, especially as they become operational. This has been the precedent set by private launch companies such as SpaceX, Blue Origin and Rocket Lab, who have been making progress developing their own new wave of re-usable launchers. To maintain the competitive edge there is no motivation or need to publish, meaning the literature base is confined to the realms of research. In response to this, an open-source approach has been proposed, where a standard geometry and trajectory is openly available to the research community to allow studies to take place outside the confines of specific projects, as well as foster collaborations between institutions with an interest in retro-propulsion in rocket systems [68,69].

The recent surge in interest in retro-propulsion technologies can be directly attributed to the success of Falcon 9, as well as the economic and environmental factors which play an important role in the sustainability of future space exploration. Reusable launchers incorporating retro-propulsion strategies have demonstrated a dramatic reduction in launch costs while achieving launch frequencies 10 to 20 times higher than expendable launchers [70]. Despite these well known advantages, the use of retro-propulsion introduces a set of complex engineering challenges. Aerodynamic considerations, such as the interaction of retro-propulsion plumes with the vehicle structure and control surfaces [36], demand careful analysis to ensure stability and controllability during descent. Moreover, the thermal loads generated during the retro-propulsion phase require a thorough understanding of the heat distributions so that suitable thermal management systems can be designed to protect the critical components of the vehicle [39].

Predicting the vehicle aerodynamic characteristics and thermal loads presents a distinct set of challenges for ground based facilities, as well as numerical simulations [71]. For wind tunnel test campaigns, the significance of achieving flight Reynolds numbers for the vehicle aerodynamics is complemented by the importance of ensuring the plume is representative of flight conditions through the use of various similarity parameters [10]. However, constraints associated with model size due to test section dimensions, as well as static conditions achieved in the test chamber, do not allow flight conditions to be exactly realised. In addition, accurate plume simulation using sub-scale models adds significant complexity to the model design, as well as place extra demands on facility infrastructure. Achieving nozzle exit conditions in a wind tunnel model that accurately simulate flight-representative thermal loads is ideal, but presents significant challenges [46]. This is mainly due to extreme temperatures experienced by the model, as well as safety concerns for the facilities themselves due to the presence of active flames or the types of species present in the exhaust [14] . On the numerical side, Reynolds similarity is no longer an issue, but the numerical approach to the problem becomes more important. Steady-state RANS simulations are by far the most cost effective way to investigate the vehicle over the entire return-to-earth trajectory, but the sensitivity of surface pressures, global aerodynamic coefficients and surface heat loads to turbulence model selection can be high [39]. In addition, during phases of flight where multiple engines are active, the plume behaviour is highly unsteady [42] and more suited to scale resolving methods such as LES. The selection of chemistry model to account for the reactions taking place around the vehicle can also influence the surface heating results and aerodynamic coefficients [16]. Finally, the significant disparity between fluid mechanical and structural time scales makes unsteady CFD analysis with structural coupling across the entire trajectory practically unfeasible. This challenge necessitates the development of fast-response models for aero-thermodynamic heating. This requirement can be met through the creation of an aero-thermal database (ATDB) [52], which serves as a surrogate model for aero-thermodynamic heating, composed of a series of steady-state CFD results for surface heat fluxes. These CFD simulations are conducted at various trajectory points, engine operational conditions, and surface temperatures. Interpolation algorithms are used to estimate the local heating rate at each point on the vehicle's surface based on flight time and local surface temperature. This surrogate model for aero-thermal loads can be easily integrated with a structural response model to evaluate the temperature history at each location on the vehicle's surface throughout the entire atmospheric flight. Aerodynamic data is derived from the same numerical simulations conducted for the aerothermal data and is often supported by wind tunnel test campaigns [38]. However, the key problem for both aerodynamic and aerothermal databases is absence of any publicly available test cases which provide flight test data where retro-propulsion is taking place. This makes the validation and assessment of uncertainties for numerical and experimental results extremely difficult.

In this review article, an overview of the current system architectures and flight trajectories of vehicles utilising retro-propulsion as a descent strategy is given. This will be followed by an examination of the existing literature on the flow field characteristics and aerothermal environment during phases of flight with active retro-propulsion. The sensitivity of heat loads to the flight state and configuration of the vehicle will also be evaluated. Next, the current capabilities and limitations of wind tunnel testing from the perspective of suitable facilities, model design and critical similarity parameters will be explored, as well as the role numerical tools play in complementing experimental campaigns. To conclude the paper, a summary of the outlook and potential research needs will be given. This is largely focused on the requirement for full scale flight test data to allow validation of both experimental and numerical datasets, as well as provide some feedback on uncertainty bands for heat fluxes and aerodynamic coefficients.

2. System architectures and mission profiles

2.1. Expendable vs. re-usable designs

The original partially re-usable launcher utilising a VTVL mission profile was the SpaceX Falcon 9. It is an evolution of the expendable Falcon 9 v1.0 and was the first launcher of its size to demonstrate the feasibility of landing the first stage for refurbishment and re-use. This launch system is a good example of the fact that fundamentally, a rocket utilising a first stage recovery strategy is very similar to an expendable equivalent. The core hardware necessary for a booster to complete an expendable flight can be narrowed down to three main elements. Firstly, a structure to house the fuel tanks, system components and carry a payload. Secondly, a propulsion system with sufficient thrust to deliver an upper stage to a predetermined altitude. Finally, a guidance system able to alter the vehicle attitude through thrust vectoring or reaction jets, to ensure the vehicle follows the correct trajectory. The pre-existence of these systems in an expendable booster means that a large amount of the existing infrastructure can be used to allow a successful retrieval of the first stage through a controlled landing, with the addition of some extra components. Falcon 9 has demonstrated the successful implementation of legs to allow the booster to stand without the need for any external support structures after landing. The legs are covered by an aerodynamic fairing and are folded close to the body during the majority of the flight. This is to ensure their contribution to the total vehicle drag is minimised, as well as to reduce mechanical loads on the linkages. The legs are extended seconds before touchdown when the vehicle velocity is low and their large spans enable the slender booster to stand with minimal tip-over risk. To guide the vehicle during its return to earth phase of flight, deployable aerodynamic control surfaces and reaction jets are required to induce pitch, roll and yawing moments, while large changes to the vehicle velocity or trajectory are initiated using the propulsion system. The specific extra requirements of the propulsion system are covered in Section 2.3. Fig. 4 shows that the re-usable variants of each Falcon 9 family (left hand side) are the same as the expendable design (right hand side), with the aforementioned additional components. Note that it is critical to distinguish the difference between a first stage landing and a first stage recovery. A landing implies that the vehicle returns to a designated landing pad and is either held upright by external infrastructure (tower catching mechanism) or stands without assistance (landing legs), while a recovery suggests methods such as in air capturing or a booster splashing down in the ocean. Therefore, a first stage recovery scenario would not necessitate the addition of landing legs or deployable control surfaces as has been discussed thus far. Successful recoveries have been demonstrated by the Space Shuttle solid rocket boosters [72] and more recently, the Rocket Lab Electron launcher [73], which both opted for parachutes to slow the boosters before splashing down.

Fig. 4. Illustration of the Falcon 9 launch system showing the re-usable variant directly next to the expendable model (Lucabon based on work of Markus Säynevirta and Craigboy and Rressi), CC BY-SA 4.0, via Wikimedia Commons.

2.2. Typical trajectories with retro-burn applications

Depending on the mission and payload, there are two options for a first stage landing. The first is a scenario where the booster is flown back to land in an area close to the launch pad and is called a return to launch site (RTLS) trajectory. After stage separation, the vehicle performs a flip manoeuvre to orient the engines downrange, before initiating a boostback burn. This needs to occur rapidly to minimise the downrange distance travelled by the booster after staging. This burn reverses the horizontal component of velocity while keeping the vertical component of the velocity more-or-less unchanged. As aerodynamic drag is minimal due to the low densities at high altitudes, the booster continues towards a typical apogee of about 130 km, before beginning its return to earth. A re-entry burn is required to reduce the velocity of the vehicle and also to shield components from high heat loads. After the entry burn is completed, the vehicle glides towards earth, before the landing burn is initiated and the booster touches down on the landing pad. A visualisation of this flight can be seen in Fig. 5. The second scenario is a downrange landing (DRL), where instead of initiating a boostback burn after stage separation, the booster follows a ballistic trajectory up to a typical apogee of around 130 km. Along this coasting phase of flight, the first stage also performs a flip manoeuvre such that the vehicle begins its journey back to earth flying backwards. The first stage then starts its descent, initiates a re-entry burn, before gliding down towards the barge located at sea and performing a landing burn for a precision touchdown (see Fig. 6). Details relating to specific flight phases of both DRL and RTLS trajectories from a mission engineering perspective are given by De Zaiacomo et al. [74].

A comparison between the DRL and RTLS trajectories in terms of altitude and velocity for the Falcon 9 are presented in Fig. 7. These represent two flown missions which have been digitised [68] and is also representative of typical flights for other research configurations [30]. While the maximum altitudes for these two missions are similar, the velocity profiles vary considerably. For the RTLS flight, stage separation occurs approximately 10 s earlier than for the DRL, resulting in a lower peak velocity of the booster. In addition, the boostback burn further reduces the magnitude of the first stage velocity by reversing its downrange component. This leads to significant reductions in pre re-entry burn velocity as well as for a majority of the aerodynamic glide phase. In both cases the landing burn is initiated at an altitude of approximately 2–3 km and a velocity of 250 m/s.

An overlay of the dynamic pressure and an empirical estimate of stagnation heat flux using the Champman equation [75] for both trajectories is presented in Fig. 8. Due to the significantly lower flight speeds

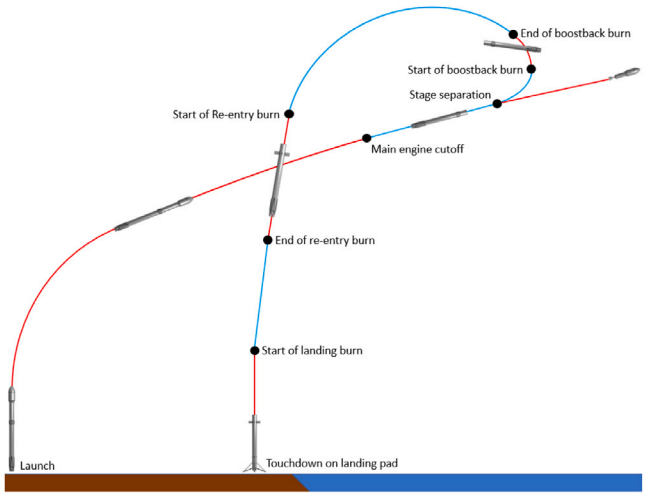

Fig. 5. Illustration of return to landing site trajectory with red signifying powered phases of flight and blue unpowered.

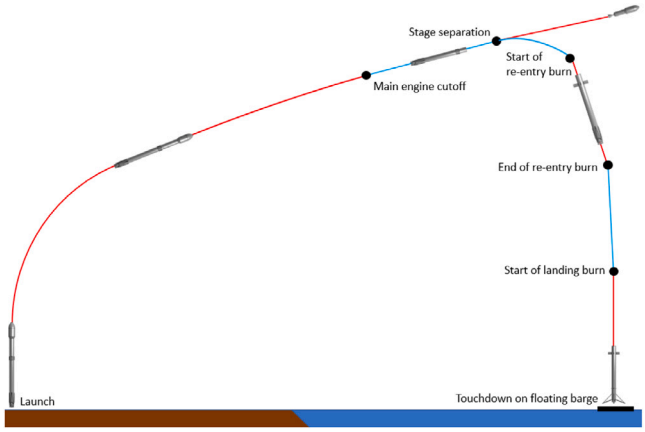

Fig. 6. Illustration of downrange landing trajectory with red signifying powered phases of flight and blue unpowered.

for a RTLS trajectory, the critical case for heating and aerodynamic loads is associated with the DRL case. Here, heat loads can be expected to be around four times higher, while aerodynamic loads are greater by a factor of almost two. As a general rule the aerodynamic loads scale with dynamic pressure (velocity squared), while the heat loads are related to the cube of velocity. Note that these predictions are only valid for flight regimes without retro-plumes. When engines are active, the booster is flying through its own exhaust which alters the temperature, density and velocity experienced in the near field of the vehicle.

For both the DRL and RTLS trajectories, there is a maximum payload capacity penalty when compared to an expendable launcher. This is a direct result of the requirement for re-usable boosters to carry extra fuel for retro-propulsion manoeuvres, as well as include the additional systems which have been discussed in Section 2.1 . Intuitively one can conclude that the RTLS trajectory which performs three burns requires more fuel onboard compared to the DRL which only executes two burns. Estimates for the reduction in payload are approximately 20% and 40% when compared with the payload performance of an expendable configuration versus a DRL and RTLS trajectory respectively [76]. A DRL trajectory is therefore viable for missions where a large payload is being launched and the required delta V at stage separation places the vehicle too far downrange for a feasible RTLS mission. Conversely, lighter payloads permit carrying extra fuel reserves, making the RTLS trajectory a viable option.

An overview of a generic vehicle highlighting the different vehicle configurations seen during both RTLS and DRL trajectories is given in Fig. 9. The variety in the vehicle layout combined with the different active nozzles during the flight mean that heat loads on components, as well as individual contributions to the overall aerodynamic coefficients, can change significantly during the duration of the mission.

2.3. Propulsion system requirements

From the perspective of propulsion system design, there is a requirement for engines to have throttling and re-light capabilities, which is not a feature of an expendable rocket. This forces the vehicle to make use of liquid fuels rather than solid propellants. The driver behind the emergence of clustered nozzle arrangements, similar to that seen in Fig. 10, is the significant change in mass experienced by the first stage throughout the flight. All nine engines are required during the ascent phase of a typical Falcon 9 flight to provide maximum thrust, accelerate the fuel laden vehicle and achieve the correct delta V at staging. At this point, the second stage jettisons the booster which only has a small fraction of fuel remaining, making the total mass of the first stage significantly lower than at launch. This means that to achieve the correct velocity after a boostback or re-entry burn, only three engines are required to be lit. Furthermore, during the landing phase only the central engine is ignited to decelerate the vehicle for a controlled landing. During the final stages of landing, the flight speed of the vehicle becomes so low that the dynamic pressure is insufficient for the control surfaces to create aerodynamic forces [53]. The centre nozzle which is capable of thrust vectoring keeps the booster vertical prior to touchdown. The ability of the nozzle to gimbal during flight is critical for controllability [77], especially during the final seconds of flight.

2.4. Vehicle control

During flight the booster achieves altitudes which place it firmly in the rarefied regime. Despite the vehicle travelling at velocities up to 2 km/s, the air density at high altitudes results in a dynamic pressure of almost zero, rendering aerodynamic control surfaces ineffective. As a result, vehicle attitude control at high altitude can only be achieved with the propulsion system or reaction control jets [78]. These jets are placed strategically at locations far away from the vehicle centre of gravity (CoG), such that moment arms are as large as possible to allow short pulses of gas to have maximum effectiveness in pitch, roll and yawing moment induction. As the vehicle decends to lower parts of the atmosphere, air density increases and the aerodynamic controls become effective. There are two main types of control surfaces which can be used for guiding the vehicle during the descent phase of flight. The Falcon 9, Super Heavy booster and Themis demonstrator make use of grid fins, while competitors Blue Origin and Rocketlab, as well as planned test vehicles such as Callisto are equipped with planar fins. Grid fins, also referred to as lattice wings or lattice controls, are compact structures comprised of multiple interconnected aerodynamic surfaces, visually similar to a lattice. This construction forms a versatile aerodynamic device capable of serving as an aerodynamic stabiliser, lifting element, or control surface. Each individual member typically takes the form of a thin, high-aspect-ratio rectangular wing with a consistent chord. Their construction can be described using various geometric parameters such as span, height, chord, member thickness, and cell spacing. An example of the Falcon 9 grid fin is shown below in Fig. 11. Grid fins offer a multitude of advantages compared with traditional planar wings [79]. For example, they are able to provide high aerodynamic effectiveness for their given low weight and volume as well as favourable performance over a wide range of Mach numbers and deflection angles. Their design also results in small hinge moments and a relatively constant centre of pressure location, which means weight and space can be saved on the actuation devices. Finally, their

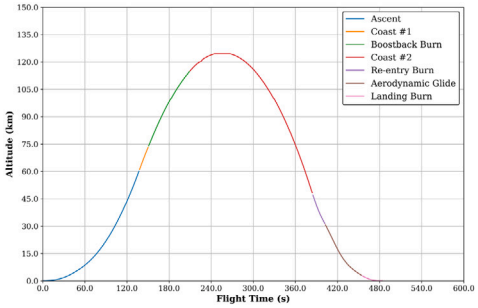

(a) Altitude vs time for RTLS

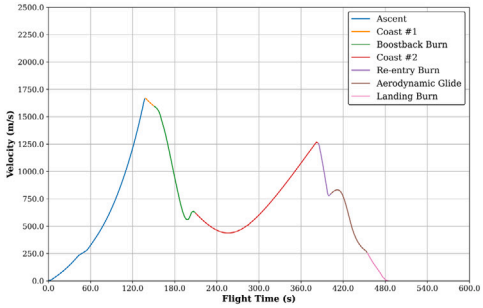

(b) Velocity vs time for RTLS

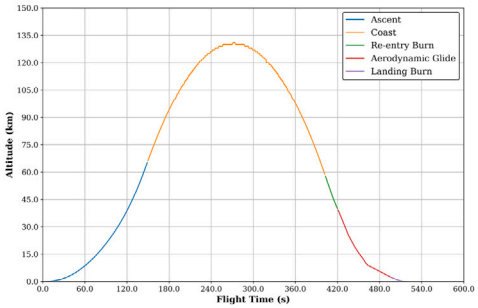

(c) Altitude vs time for DRL

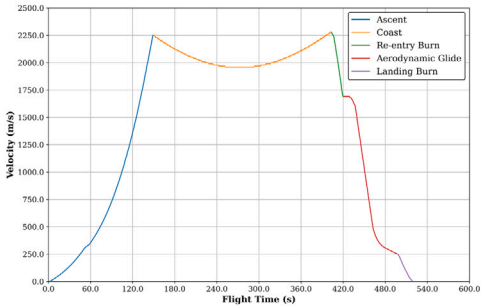

(d) Velocity vs time for DRL

Fig. 7. Comparison between DRL and RTLS trajectories [68].

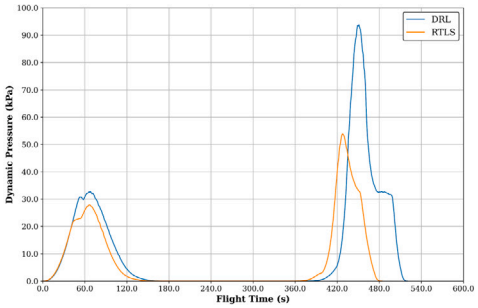

(a) Dynamic pressure vs time

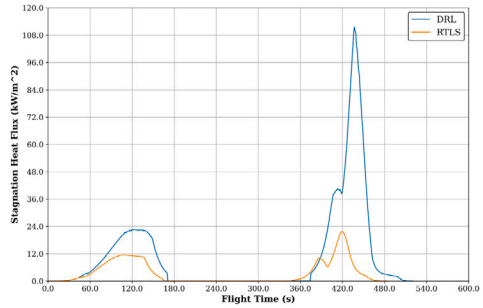

(b) Stagnation heat flux vs time

Fig. 8. Dynamic pressure and approximate stagnation heat flux for both DRL and RTLS trajectories assuming no retro-plume.
Source: Calculated from [68].

compact size allows them to be folded easily when not required, making the booster compact with little additional drag during the ascent phase. They are however not without disadvantages, with the main being the existence of a critical Mach number, where normal shock waves occur in some or all of the grid cells, resulting in a choked flow. This causes dynamic instabilities which can strongly influence the induced pitching moment on the vehicle [80]. The low aerodynamic efficiency when deflected has a positive effect on the booster as it aids in stability during descent [81]. On the other hand, traditional planar fins have been shown to be more effective in generating normal force compared to grid fins, but at the expense of larger actuation forces and overall planform area [82,83].

Recently, here has been some work on developing novel aerodynamic control solutions. An example of this is the use of an unfoldable inter stage segment, also known as petals, for vehicle trim, control and drag generation (see Fig. 12). Such a design is extremely attractive because it removes the need for external control surfaces and utilises existing infrastructure. However, load analyses concluded that the mass of each petal segment was too high. Moreover, the mass of the actuators required to move the petals during the flight was excessive. This rendered this design unfeasible and a more traditional planar fin design was selected [29].

2.5. Future trends for vehicle design

At present, there are four established launch providers which are actively developing new, re-usable vehicles. Ariane and ESA are pushing ahead with the Themis demonstrator, which represents the first attempt at developing a large scale, re-usable booster in Europe. The SpaceX Starship and Super Heavy booster are deviating somewhat from the Falcon 9 design, with a fully re-usable upper stage, an increase in the number of engines in the cluster, as well as a tower catching mechanism eliminating the need for landing legs [84]. Rocketlab and Blue Origin appear to be breaking ground in new booster designs representing a deviation from SpaceX. The Blue Origin New Glenn as well as the Rocket Lab Neutron have recessed nozzles within the base area, presumably to alter the base flow, reducing the thermal and aerodynamic loads. Additionally, the use of an integrated second stage

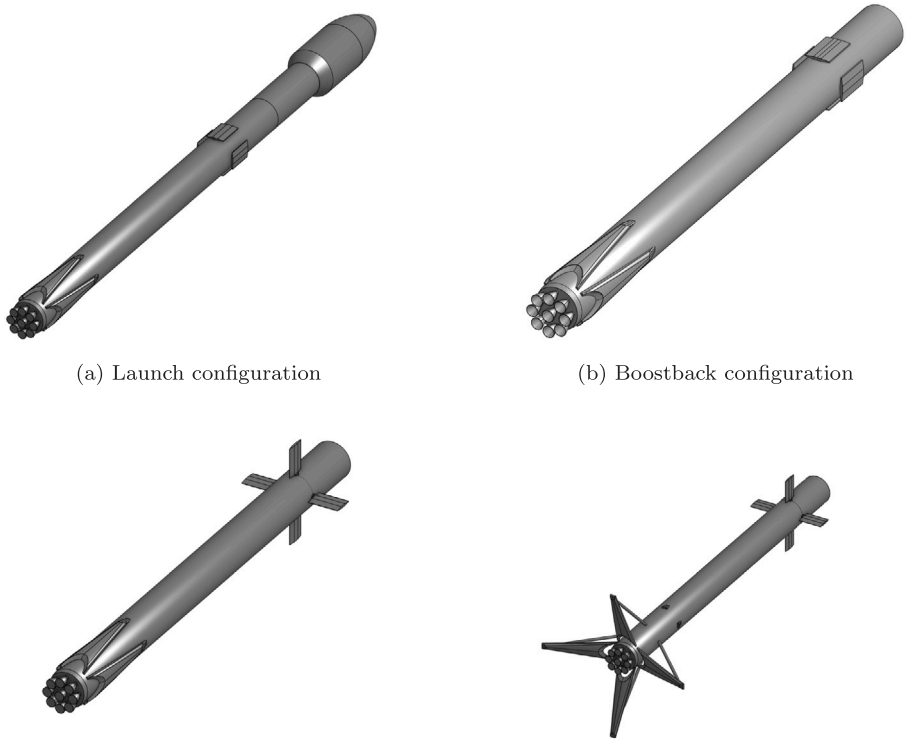

(a) Launch configuration (b) Boostback configuration

(c) Re-entry and glide configuration (d) Landing configuration

Fig. 9. Various vehicle configurations through ascent to re-entry and landing [69].

Fig. 10. Illustration of cluster arrangement where 8 peripheral nozzles surround a central nozzle (SpaceX Photos, CC0, via Wikimedia Commons).

Fig. 11. Deployed grid fins on a Falcon 9 booster (Steve Jurvetson, CC BY 2.0, via Wikimedia Commons).

and increased base area stand out as unique design features of the Neturon vehicle [85]. However, all vehicles feature forms of strakes towards the base of the body, which will be used for lift generation and improvement of cross-range capabilities [86], potentially requiring less fuel to be burned during retro-propulsion maneouvres. Strakes are not a new concept and have been successfully implemented in fighter aircraft such as the F-18 [87], and become more effective as angle of attack (AoA) is increased past 10 degrees [88]. This is due to the vortex lift phenomenon, where the sharp leading edges of the strakes promote flow separation and the formation of a vortex [89,90]. This suggests that this next generation of vehicles may be flying at AoAs greater than 10 degrees, which is the upper limit of AoA typically investigated for the Falcon 9 type boosters [38,45].

Another example of the shift in design methodologies is the choice of methane for all the vehicles. Boosters powered by liquid fuel have a rich history of utilising kerosene as their propellant, a mixture of various hydrocarbons. This fuel, known as T(S)-1 in Russia and RP-1 in

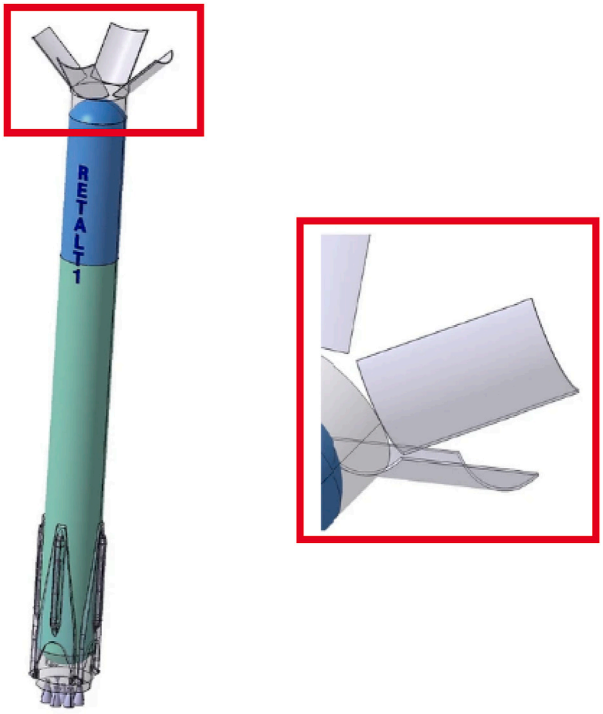

Fig. 12. Concept using unfoldable interstage bay petals.
Source: Adapted from [29].

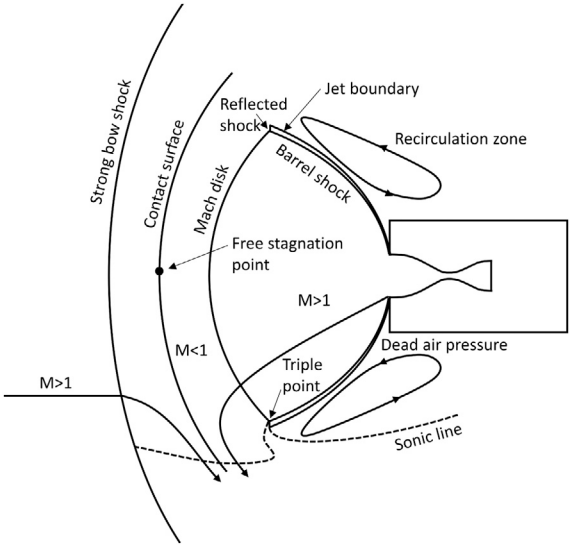

Fig. 13. Short or blunt penetration mode for supersonic flight simulating high altitude.
Source: Adapted from [100].

the USA, has been employed extensively for many decades because its high propellant density facilitates a compact design of turbomachinery and small stage sizes [91]. The motivation to consider methane for re-usable launcher applications is driven by factors such as lower soot production [92], which will reduce the heat flux in the base area due to radiation. Methane also has a higher coking limit [93], which results in less solid deposits occurring within the engine and should significantly reduce the cost of refurbishing the engines between flights. Additional benefits such as higher specific impulse, lower pressure drop in cooling channels and superior cooling properties compared with kerosene [94,95] have also been discussed in literature.

Finally, it is worth mentioning that some limitations of traditional bell nozzles have been identified, particularly with reference to high altitude operation of the first stage engines during boostback or re-entry burns. It has been postulated that the use of advanced nozzle concepts such as aerospikes, dual bell and expansion–deflection nozzles could provide performance gains of up to 15% due to their altitude compensation abilities [96]. While the combination of both vacuum and sea level variants of the Raptor engine on SpaceX Starship highlights the fact that optimal expansion ratio engines for different stages of flight is being considered, advanced nozzle concepts present too much of a risk for industry at this time. Further investigations into the advantages and disadvantages of these less traditional approaches continue within the realms of research [97,98].

3. Flow field characteristics and aerothermal environment

3.1. Single plume structures

When considering a single retro-plume, the shape and general structure seen during flight is highly dependent on the nozzle exit conditions, the freestream static and dynamic pressure, as well as Mach number. During hypersonic or supersonic retro-propulsion manoeuvres, there are two plume types which have been observed in the literature. The first is the blunt or short penetration mode and the second is the long penetration mode [10,99]. For a single active engine, the blunt mode is characterised by a underexpanded plume as seen in Fig. 13. The underexpansion is not due to the freestream Mach number, but rather the fact that hypersonic and supersonic retro-propulsion burns tend to occur at high altitudes where the pressure around the base of the rocket is significantly lower than the pressure at the nozzle exit plane. For this condition, a large degree of plume spreading is observed, with the flow exiting the nozzle meeting the oncoming freestream at a contact surface. When the freestream is supersonic, a strong shock forms upstream of the contact surface (relative to the jet flow), which decelerates the flow to subsonic Mach numbers. A region of recirculation forms behind the plume, with the pressure measured in this area called the dead air pressure. This is a critical parameter which is discussed later in Section 4.2. Fig. 14 illustrates the long penetration mode of a single jet encountering a supersonic freestream. This mode is characterised by an overexpanded plume, where a series of reflected shocks follow an initial incident shock. The long penetration mode is an unstable flow field where the jet plume penetrates the bow shock, reducing its strength [99]. Regions of recirculating flow are observed along the length of the plume, which are caused by the redirection of the nozzle flow at the free stagnation point. During the landing burn, where the freestream Mach number is subsonic and the atmospheric pressure is high, a typical overexpanded, multi-cell plume structure, is also observed. This is similar to the long penetration mode, but without the presence of any bow shock. In these cases, the axial momentum of the freestream is reduced, allowing the jet to penetrate longer into the freestream [35].

3.2. Multi-plume structures and plume-plume interactions

For orbital class launchers, entire retro-propulsion burns with a single active nozzle are typically restricted to the landing phase [30,43], with the bulk of literature focused on multi-engine burns and the resulting flow field [36,39,41,42]. For a re-usable booster, a nozzle cluster arrangement has been proven to be effective for Falcon 9, where 3 engines are lit during re-entry and a single engine is ignited for landing. The SpaceX Super Heavy booster, which has a significantly larger dry mass than any of the aforementioned launchers, uses a triple ring arrangement, where 20 Raptor engines are placed in the outer ring, 10 in the middle ring and 3 at the core. Based on images seen during the construction of the booster, it has been speculated that a

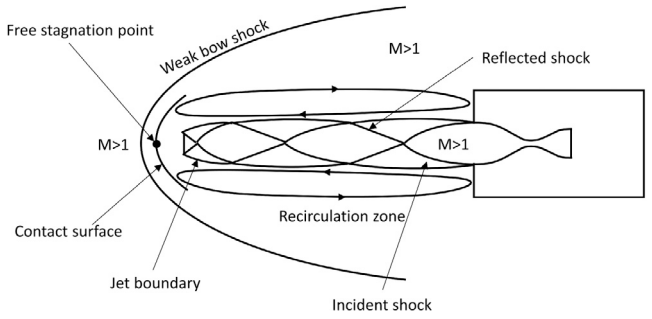

Fig. 14. Long penetration mode.
Source: Adapted from [99].

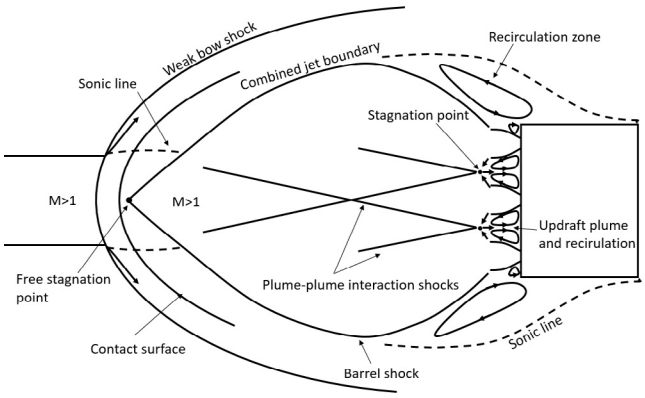

Fig. 15. Plume-plume interactions during supersonic backward flight.
Source: Adapted from [106].

separate tank used for landing feeds the inner two rings of engines, meaning a landing burn could be performed using between 3 and 13 engines [101]. The boostback and landing burns seen during the fourth test flight of Starship confirmed this suspicion [102]. While the typical investigations which appear in the literature are more focused on Falcon 9 like geometries, other studies have focused more on generic configurations with a variations in the number of engines to understand more fundamentally how the flow topology in the base region is influenced by the number of engines, as well as their layout [103].

Plume-plume interactions can arise at any time during a flight where multiple engines are active, regardless of ascent or descent [39,45]. The amount of interplay the exhaust gases have with each other is strongly dependent on the exit pressure ratio (EPR), which is the ratio of the exit pressure at the nozzle outflow plane to the static pressure field around the base region of the rocket. It is important to note that this base pressure is not necessarily the ambient pressure [100], as during flight there may be variances in the base static pressure due to geometric features causing shocks to form or for flow to separate. The EPR is also a key similarity parameter for wind tunnel experiments which will be discussed later in Section 4.2.

Interactions between plumes can be easily described by considering a booster with a clustered nozzle arrangement during launch, where an observer notices what looks like a single, thick plume, rather than multiple separate jets. This is despite the fact that the plumes at the nozzle exit are characteristically thin due to the high ambient pressure causing an overexpanded structure. This causes the interactions between exhaust jets to occur significantly downstream of the nozzle exit plane. This is however not the case during high altitude operation, where the EPR is higher than at low altitude and the exhaust becomes underexpanded. In a plume comprised of multiple underexpanded jets, the flow topology becomes quite complex [104,105].

Fig. 15 shows a three nozzle configuration during a supersonic retropropulsion burn at high altitude. Radially expanding plumes from neighbouring nozzles interact downstream of the nozzle-exit plane. This creates local stagnation regions where the hot exhaust gases are deflected towards the baseplate, resulting in a reverse flow known as the updraft plume. This causes a re-circulation region between the nozzles. These gases then escape through the unobstructed areas between the peripheral nozzles. Within the combined plume, shocks caused by the interactions between individual jets are observed. Further downstream of the nozzle exits a bow shock forms. The freestream meets the nozzle flow, resulting in a free stagnation point. Both the freestream and exhaust gases mix and are redirected around the plume following the combined jet boundary along the contact surface, before separating off the leeward side of the plume [106].

While Fig. 15 presents a simple overview of the interactions present during a high altitude, multi-engine retro-propulsion burn, it should be noted that experimental investigations have shown that the plume is in fact highly unsteady. Fig. 16 highlights the difference between steady-state CFD compuations which predict a long penetration mode and the mode switching which takes place between short penetration and long penetration modes seen in the wind tunnel [42]. Comprehensive analyses of the RETALT configuration concluded that the cause of the fluctuations in the plume are most likely not caused by outer flow interactions, but rather the jet itself [36].

3.3. Aerothermal environment during retro-burns

As already discussed, retro-propulsion for orbital class launchers can occur during the boostback, re-entry or landing phase of flight. Almost the entire boostback burn typically occurs out of the continuum range and as a result, there is no existing literature outlining numerical or experimental work for this phase of flight. For the booster re-entry, results from a range of CFD investigations highlight the numerous gas dynamic effects which are present [39,45,71]. This is due to the already discussed plume-plume interactions which influence baseplate heating, as well as the interaction of the plume with the hypersonic freestream. As an illustration, results from a steady-state CFD computation at 63 km altitude encountering a Mach 7 freestream is shown in Fig. 17.

The plume displays a distinctive barrel shock and a Mach disk. Analysis of the flow field reveals that the presence of the plume induces the formation of a detached bow shock far upstream of the exhaust plume. This effectively shields the base of the vehicle from direct exposure to the high-energy incoming free stream, safeguarding its components. Fig. 18 presents results from two isothermal wall temperatures at various points through the flight of the RETALT vehicle, highlighting the effectiveness of the shielding provided by the retro plume. It can be seen that the critical case for baseplate heating occurs shortly after engine shutdown [39].

As the free stream air passes through the bow shock, it is redirected by the jet plume, creating a contact surface between the exhaust and the air in the stagnation zone. This interaction is marked by a temperature gradient observed between the Mach disk and the bow shock, delineated by the brown exhaust boundary. The high EPR leads to the plume-plume interactions discussed in the previous section, where interaction shocks form. While Fig. 17 gives a good initial overview of the flow field during the re-entry burn, it is only a snapshot in time. It is important to consider that the re-entry burn typically only lasts in the tens of seconds and the booster can travel at speeds between 1 to 2 km/s. As a result, altitude drops somewhere between 20 and 30 km, which results in a significant difference in freestream conditions when the burn is first initiated, compared to when it is terminated [39]. This gives rise to significant variations in parameters such as dynamic pressure and EPR throughout the burn, which directly correlate the degree of plume spreading, as well a plume penetration length. The plume is still in an underexpanded state for both cases, but the degree

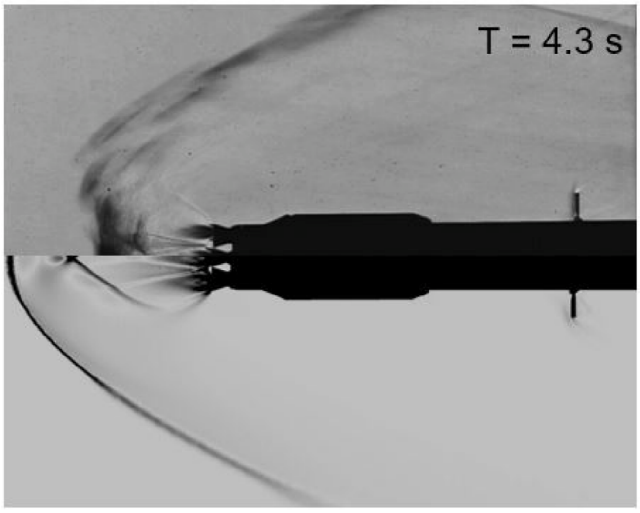

(a) Multi-Engine burn short penetration mode

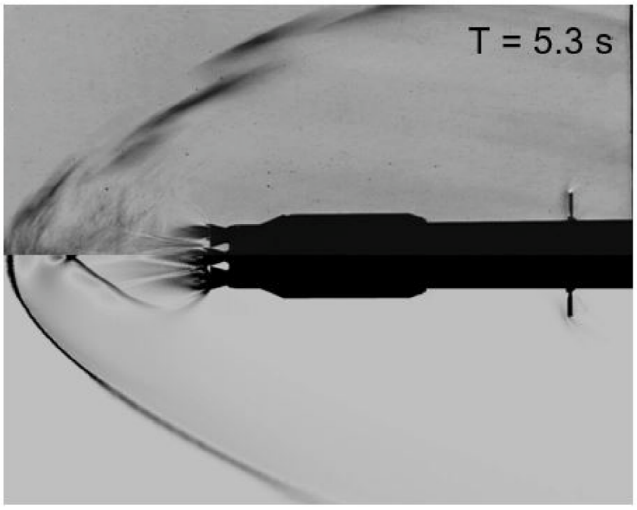

(b) Multi-Engine burn long penetration mode

Fig. 16. Two modes observed during wind tunnel tests conducted at Mach 5.3 compared with steady-state CFD during the RETPRO project [42].

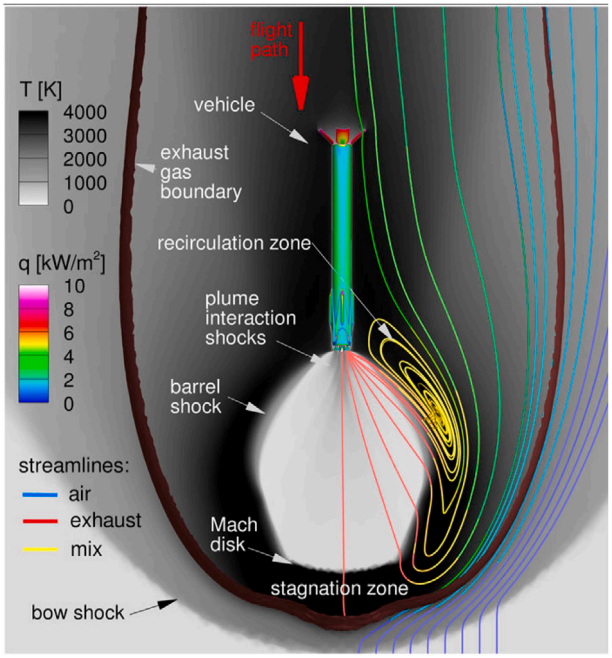

Fig. 17. Typical flow structure during a retro-burn manoeuvre during hypersonic re-entry [71].

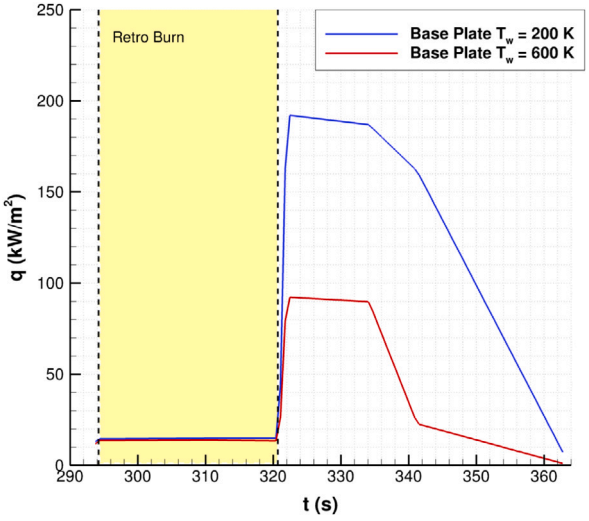

Fig. 18. RETALT1 time histories of average heat flux for baseplate constant wall temperatures — descent phase [39].

of post expansion is significantly reduced at the lower altitudes as can be observed in Fig. 19.

It can be seen that the larger plume at the top of the burn results in increased recirculation behind the plume, compared with the end of burn scenario. The highly spread exhaust also shields the whole vehicle very effectively from the oncoming air. The coloured streamlines give insight into the degree of mixing that occurs between the freestream air and the engine exhaust, where a clear correlation between increased mixing and size of recirculation zone size is observed. Surface heat flux results also show that the lower Mach number case at the end of the retro-burn has higher heat fluxes than at the top of burn. This is directly related to the flow density and velocity, where the 63 km altitude case has a low freestream density mixing with the low density exhaust gases. This, combined with the plume shielding, results in comparatively low velocities around the vehicle compared to the freestream. The lessened plume shielding effect at the lower altitude allows the freestream to maintain a high velocity and the lower degree of mixing combined with higher atmospheric density gives a significant increase in surface heating [39].

The conditions experienced during landing vary significantly to the re-entry as exhibited in Fig. 20. The first main difference is that the freestream Mach number is trans-or-subsonic. As a result, no shock is present downstream of the stagnation point between the exhaust gases and the oncoming counter-flow. Due to the low EPR, the exhaust is characterised by a long, thin structure, as expected for an overexpanded plume. At the stagnation point, the exhaust and freestream air come into contact and resulting gas mixture then turns back towards the baseplate. This results in recirculating flow along the entire length of the plume as discussed in Section 3.1. The landing legs, control surfaces and the shoulder of the baseplate are left exposed to a static temperature a few hundred degrees higher than ambient.

3.4. Impact of the flight state and configuration on thermal loads and vehicle aerodynamic characteristics

When discussing the flight state and configuration, the first variables of interest are the atmospheric conditions as well as freestream

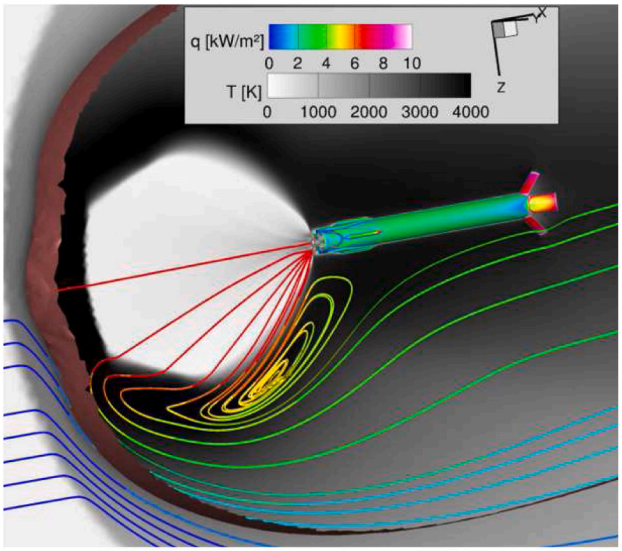

(a) Top of re-entry burn at 63 km altitude

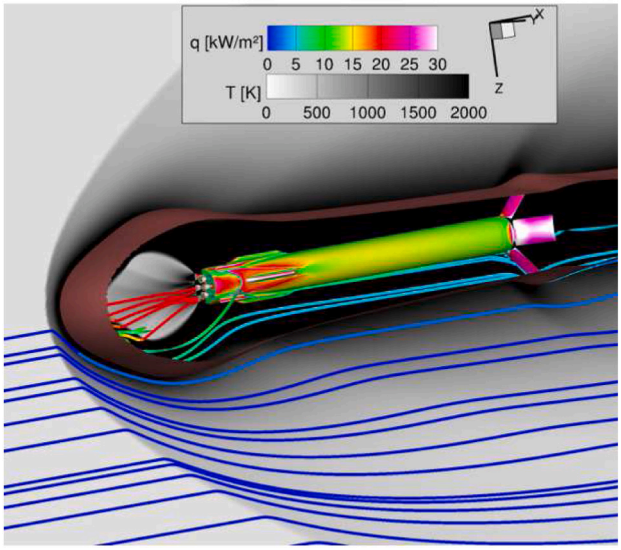

(b) Bottom of re-entry burn at 36 km altitude

Fig. 19. Steady-state CFD simulations of the RETALT vehicle during re-entry burn (streamtraces coloured according to mass fraction of the two species, air and exhaust, with red streamlines indicating 100% exhaust gases and blue indicating 100% air) [39].

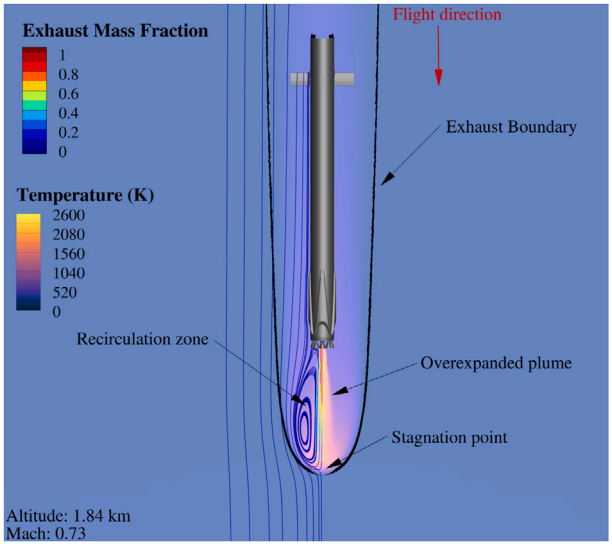

Fig. 20. Typical flow structure during a transonic landing burn [107].

Mach number. Their influence on the flow field and surface heating has been discussed in the previous section and will not be revisited here. This leaves the vehicle orientation to the airflow in terms of AoA, the type of control surfaces and their deflection angles, landing leg position, cycle type of the engines, as well as the influence of gimballing the nozzles for thrust vector control (TVC).

A re-usable first stage can be simply described as a circular cylinder, which during the return to earth phase of flight, is exposed to an axial flow with low AoA. Under these conditions, the drag of the cylinder is largely determined by the pressure on the face exposed to the freestream. This is referred to as the nose pressure and at Mach numbers above 5, contributes to approximately 90% of the total drag [108].

During a retro-propulsion burn for either re-entry or landing, high speed, high temperature exhaust gases are ejected from one or more nozzles. As has been shown in the previous sections, the flow field in the area around the baseplate is significantly augmented, with freestream flow no longer directly impinging on the baseplate. This causes a significant reduction in the aerodynamic drag of the vehicle [10,34,100], particularly at high altitudes, where a large degree of plume spreading is observed which shields the vehicle entirely. Drag has been observed to be one order of magnitude lower than what is seen during plume off conditions, with negative drag, i.e. suction, also being reported in the literature [109].

The shape of the plume has been found to be largely determined by the thrust coefficient and the drag reduction experienced by the vehicle has been shown to be dependent on this [9,11]. More fundamental investigations of plume effects on the base flow of cylinders have highlighted that the ratio of body diameter to nozzle throat diameter plays a critical role. Extreme examples of the significance of this ratio for the vehicle drag show that conditions where large body diameters are coupled with small jets, or vice-versa, significant changes in the shock structure and general base flow are observed [4].

When the vehicle flies at some AoA during a retro-propulsion phase of flight, the oncoming airflow causes the exhaust gas to be deflected towards the leeward side of the vehicle (see brown iso-surface in Fig. 21). At high AoA, e.g. 10 degrees, the windward side of the aft part of the rocket is subjected to an inflow of almost uncontaminated air, which can result in a strong pitching moment behaviour as a normal force is introduced at a point which is far away from the CoG of the booster. The length of the booster also plays a significant role in whether this phenomenon is seen. Due to the relatively high flow densities and velocities, the heat loads in this area are increased compared to a baseline 0 AoA case. The hot exhaust gases accumulate at the leeward side of the vehicle which results in a second area of increased heat loads at and around the upper landing leg cover. The base heating pattern remains unaffected by the inclined inflow as the nearfield is still dominated by the plume interaction effects as well as the efficient shielding the plume provides from the free stream [45].

From a thermal loading perspective, the most critical components are generally observed to be the leading edges of the control surfaces. This is due to the small leading edge radii which are typically used in these areas, which result in typical local peak loads of about 350 kW/m^2 and 500 kW/m^2 [39,45] (see Fig. 22). These values decrease very rapidly in the downstream direction and occur only at the windward surfaces of the leading edges. Fig. 22 also shows that with a freestream Mach number of 5.3, the grid fins see a subsonic inflow.

When the vehicle flies at some AoA, the Angle of Roll (AoR) can influence the heat load distribution on the deployable structures — the fins and the landing legs. The influence of AoR has been investigated as one of several parameters influencing heat loads on deployed landing legs [48]. It was shown for an AoA = 170 degrees and AoR = 0

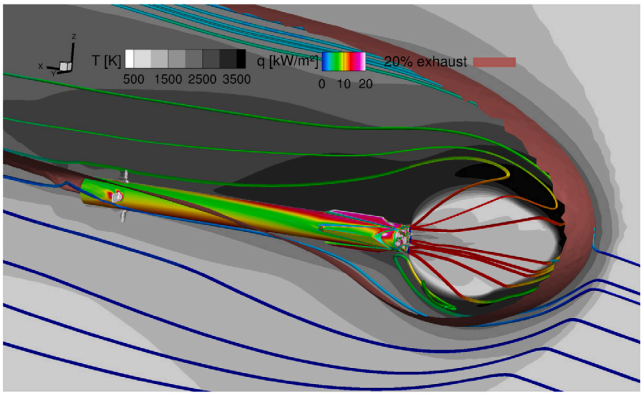

Fig. 21. Mach 5.3, AoA = 10 deg: flow field [45].

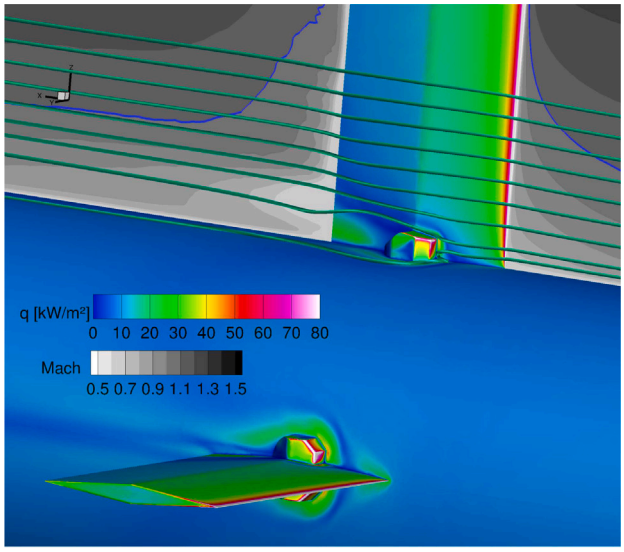

(a) Planar fin heat load

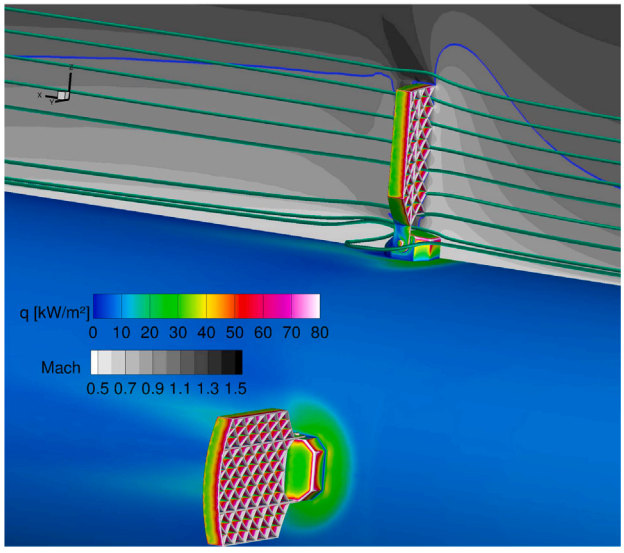

(b) Grid fin heat load

Fig. 22. Comparison between planar and grid fins during re-entry burn of the RETPRO configuration at Mach 5.3 [110].

degrees that parts of the plume are deflected onto the landing leg on the leeward side, leading to increased heat loads to that leg. Changing

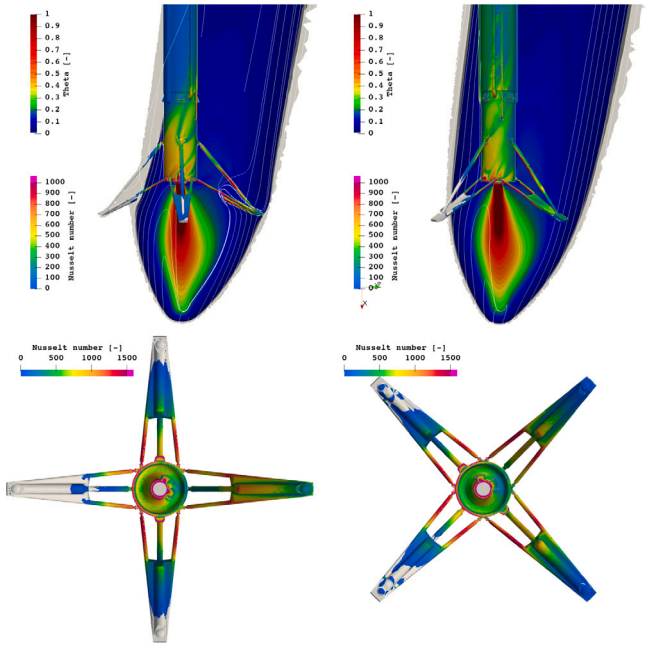

Fig. 23. Influence of angle of roll on heat loads on deployed landing legs [48].

from AoR = 0 degrees to AoR = 45 degrees, as shown in Fig. 23, leads to the vast majority of the plume now passing in between the two landing legs and thus to comparably lower heat loads. This observation is also considered relevant to the fins.

The deformation of the exhaust plume structure is similar for both AoA and TVC cases (see Fig. 24 and Fig. 21), however important differences occur. While the entire vehicle is still immersed in its exhaust gases, the TVC case is characterised by smaller changes in the main flow pattern and subsequently the heat flux distribution is less asymmetric. The overall levels are comparable to a 0 AoA and 0 TVC case. On the other hand, the inclined central jet does alter the exhaust gas recirculation pattern near the base and the hot spot at the impingement location moves in the direction of the TVC inclination. The overall flow topology remains similar as visible in the skin friction patterns. This is illustrated in Fig. 25(a). Part (b) of this Figure depicts the flow structure in the symmetry plane of active nozzles. It is important to consider that TVC is typically used as a control strategy and it is unlikely that the nozzle will be at a fixed deflection angle for long periods of time. Steady-state CFD results are therefore representative of this static deflection. In flight, the constant gimballing of the centre engine will spread the heat loads over a larger area, reducing the likelihood of a hotspot occurring in a single location.

During landing cases where the legs are deployed there are some key considerations from a thermal loading perspective. Typically landing legs are only deployed a few seconds before touchdown leading to a short exposure time for the landing legs, but with high heat loads due to the proximity of the legs to the hot plume core. The thrust level of the engines as well as the attitude of the vehicle have a strong influence on the local distribution of the heat flux on landing legs and baseplate in this configuration [48] as shown in Figs. 26(a) and 26(b).

For lower altitudes this configuration is typically investigated with the presence of a ground plane. When the vehicle is in close proximity to the landing pad, the plume impacts the surface nearly perpendicular and is redirected to flow parallel to the ground. As the nozzles are located higher than the landing leg extremities, at touchdown there is an increased heat loading from high speed, high temperature exhaust gas impingement on the landing legs. After engine shutdown, there is also the risk of high radiative loads due to the heating of the pad which occurred in the seconds before landing. Numerical investigations

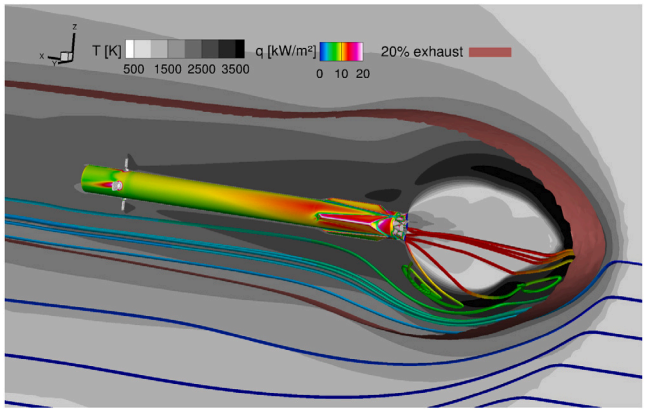

Fig. 24. Mach 5.3, TVC = 5deg: flow field [45].

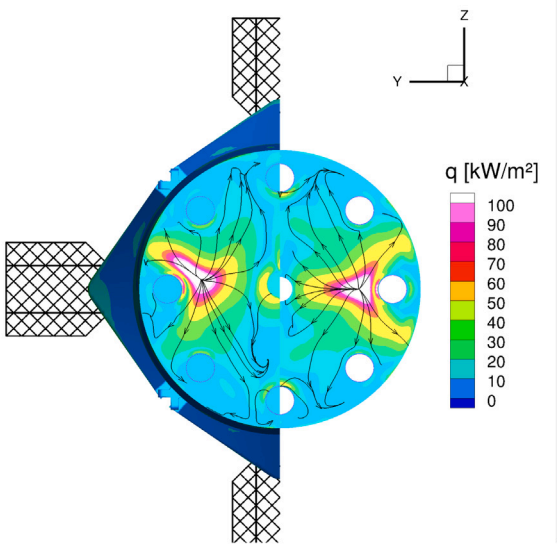

(a) Mach 5.3, TVC = 5deg: Base flow details

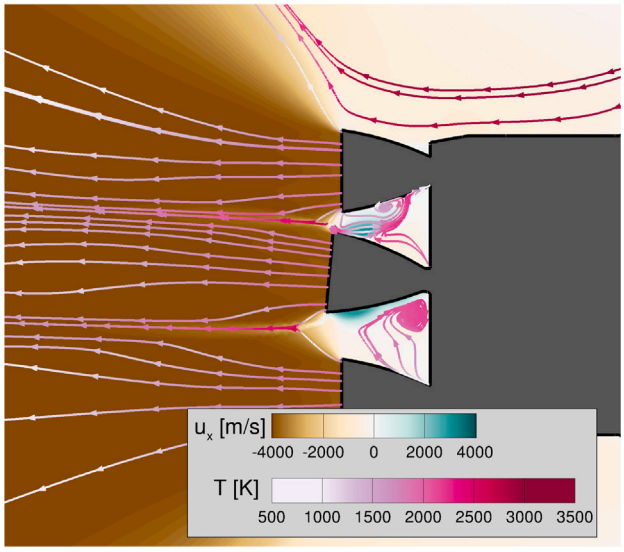

(b) Mach 5.3, TVC = 5deg: Planar fin

Fig. 25. Mach 5.3, TVC = 5deg: Base flow details [45].

of ground heat flux over nozzle distance for a single engine [63] reveal a non-linear behaviour, as shown in Fig. 27. At distances closer to the ground ($x/D = 1 - 5$) the heat flux starts to deviate from that of a classical free stream impingement jet. In the region of the stagnation point flow, below the plate shock, recirculation bubbles are formed, as shown in Fig. 28(a)–(b). In these cases the heat flux maximum is shifted off centre, occurring at the point where the slip flow from the plate shock impinges onto the ground. For distances very close to the ground ($x/D = 1 - 1.5$) a secondary maximum in the heat flux can be observed further outward in the radial direction, caused by an oblique shock inside the wall stream, which can be observed in Fig. 28(a) and (b). The highest maxima of $h > 32\,\mathrm{MW\,m^{-2}}$ do not occur at the closest nozzle to ground distance, but instead for $x/D = 5$ and $x/D = 1.5$. This is due to higher local pressures caused by the stronger recirculation in the stagnation, as can be observed well in Fig. 28(b).

Finally, the type of engine cycle can also play a role in the thermal loads experienced by the vehicle. It has been shown that the presence of a gas generator exhaust, otherwise referred to as a bleed nozzle (BN), from an open cycle engine can provide gas dynamic shielding of the baseplate [111]. The investigation was aimed at post combustion of the fuel rich secondary nozzle exhaust near the baseplate. It was found, however, that for the investigated configuration no combustion is taking place near the baseplate due to low temperatures and the local lack of oxygen. It was observed that the secondary nozzles greatly reduce the back flow from the main engines, as visualised by the $u = -200\,\mathrm{m\,s^{-1}}$ iso-contour in Fig. 29. The resulting influence on the baseplate heat flux is shown in Fig. 30. The heat flux maxima to the $T_W = 600\,\mathrm{K}$ wall decreases from over $200\,\mathrm{kW\,m^{-2}}$ to below 0. While this phenomenon has not been extensively investigated, the findings show that there could be some potential benefits from strategic placement of gas generators to reduce the amount of thermal protection required.

In summary, based on the available literature, some conclusions can be drawn with respect to trends as well as typical heat loads which can be expected during the return to earth phase of flight. The presence of secondary (gas generator) exhaust has a significant impact on the hot gas recirculation and can substantially reduce baseplate loads. The highest thermal loads on the baseplate occur immediately after shut-down of the retro-burn during entry and descent when the vehicle is exposed to the supersonic free stream. Area averaged heat loads between 200 and 300 kW/m^2 occur in this flight regime with local peaks up to 600 kW/m^2. The highest thermal loads on control surface leading edges and surface protrusions occur during the end of the retro burn (maximum atmospheric back pressure) and after shut-down of the retro burn (undisturbed supersonic free stream). Here, leading edge heat fluxes around 400 kW/m^2 are seen. Retro-burns at low altitude can produce very significant thermal loading on the vehicle surface. This is due to the high atmospheric back pressure and the associated high density of the impacting hot engine exhaust. After burning effects (increased heat load due to post-combustion of the fuel-rich engine exhaust) are especially important for hydrocarbon fuels. Close to touch down, the tips of the deployed landing legs dip in to the hot engine exhaust flow on top of the landing surface. This can cause high loads on the tips in the order of up to 600 kW/m^2.

4. Ground based testing

4.1. Applicable facilities

It has already been shown that during the return to earth flight of a re-usable booster, a velocity range of approximately 2.2 km/s all the way down to 0 km/s at landing will be experienced. This correlates to a Mach number range of interest between Mach 8 and 0. Due to the differences in flow physics of compressible and incompressible flows, design philosophies between high speed and low speed wind tunnels are generally not compatible and there is no single facility which is able to cover this range of testing conditions. As a result, separate campaigns which target specific phases of flight need to be planned, with the

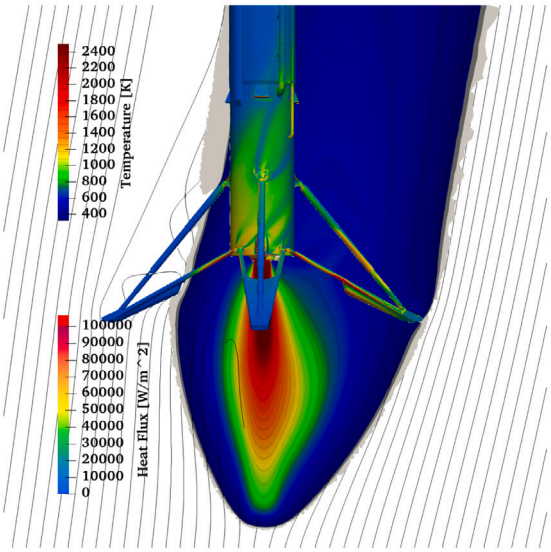

(a) Temperature field and surface heat flux, $M = 0.5$, $AoA = 170°$

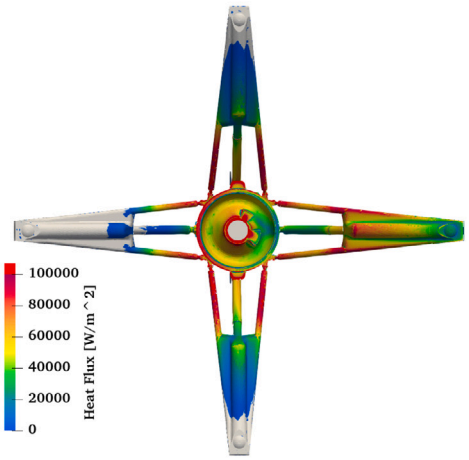

(b) Surface heat flux bottom view, $M = 0.5$, $AoA = 170°$

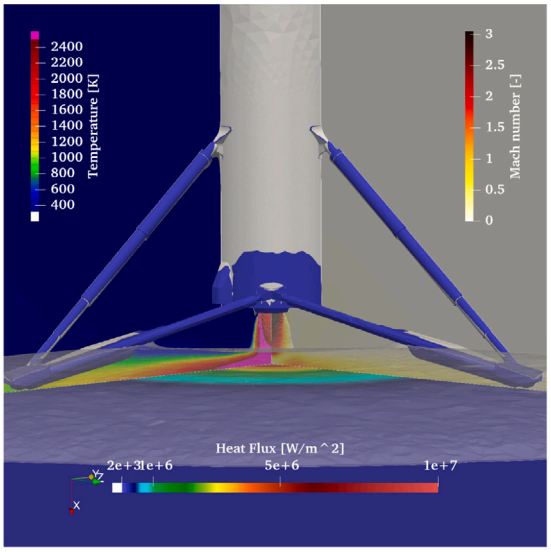

(c) Heat loads on ground (top view)

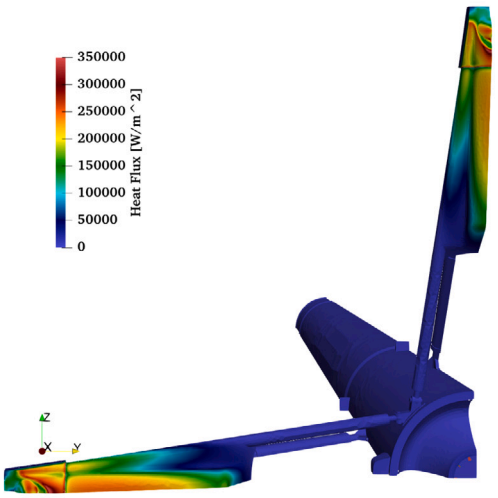

(d) Heat loads on ground (side view)

Fig. 26. Different simulation scenarios for heat loads on Callisto with deployed landing legs [48].

common trend being to divide the test campaigns according to hypersonic, supersonic and subsonic. Examples of successful test campaigns investigating both supersonic and subsonic retropropulsion burns are well documented [34,35,40,58]. Fig. 31 gives a broad outline of the types of compressible flow facilities and their applicability limits, with an overlay of various spacecraft trajectories provided. The facilities depicted here are considered to be high enthalpy, with the exception of blowdown tunnels. Traditionally high enthalpy tunnels have been used to simulate re-entry conditions experienced by vehicles travelling at speeds of approximately 2.5 to 11 km/s, which is typical for spacecraft returning from orbital or lunar missions [112]. However, the subortical trajectory flown by a first stage booster, which is characterised by lower freestream Mach numbers and stagnation temperatures, fits well within the operational range of blowdown tunnels [40].

The blowdown tunnel is a low enthalpy facility which is capable of producing high Mach number flows. As blowdown tunnels operate intermittently, test durations are typically in the realm of seconds to minutes. These longer test durations make blowdown tunnels suitable for comprehensive aerodynamic analyses, such as AoA sweeps, and for observing unsteady plume behaviour using flow visualisation techniques such as Schlieren photography [36]. An overview of a blowdown tunnel is given in Fig. 32, which shows that a nozzle upstream of the test section is used to define the Mach number of the freestream. Increasing flow kinetic energy through nozzle expansion leads to a decrease in temperature at the exit due to energy conservation principles. When testing with air and using large expansion ratio nozzles for high Mach numbers, the air must be dried and heated to prevent moisture, oxygen, and nitrogen condensation. Consequently, blowdown facilities are considered "cold" since the air temperature in the test section is kept slightly above the condensation point to prevent liquefaction during expansion, resulting in a lower speed of sound for the test gas. Thus, achieving Mach number similarity in these tunnels requires lower flow velocities, leading to reduced enthalpy and stagnation temperatures compared to actual flight conditions. If desired, increased stagnation temperatures can be achieved with high powered heaters raising the freestream temperature to be well above the condensation point [36]. However, for cases with active retro-propulsion, surface heating as well as the aerodynamic characteristics of the vehicle are largely governed

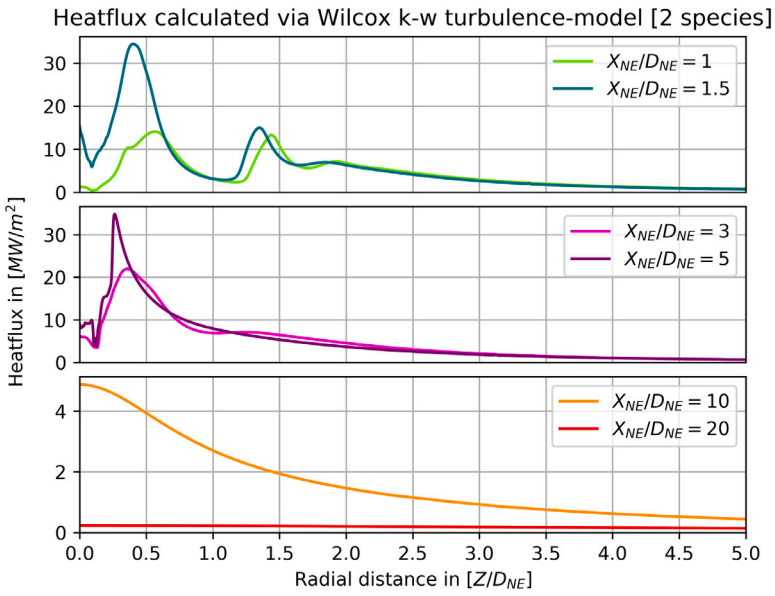

Fig. 27. Ground heat fluxes for different nozzle to ground distances: (a) x/D = 1.0, (b) x/D = 1.5, (c) x/D = 3, (d) x/D = 5, (e) /D = 10, (f) /D = 20 (D_{NE} refers to nozzle exit diameter) [48].

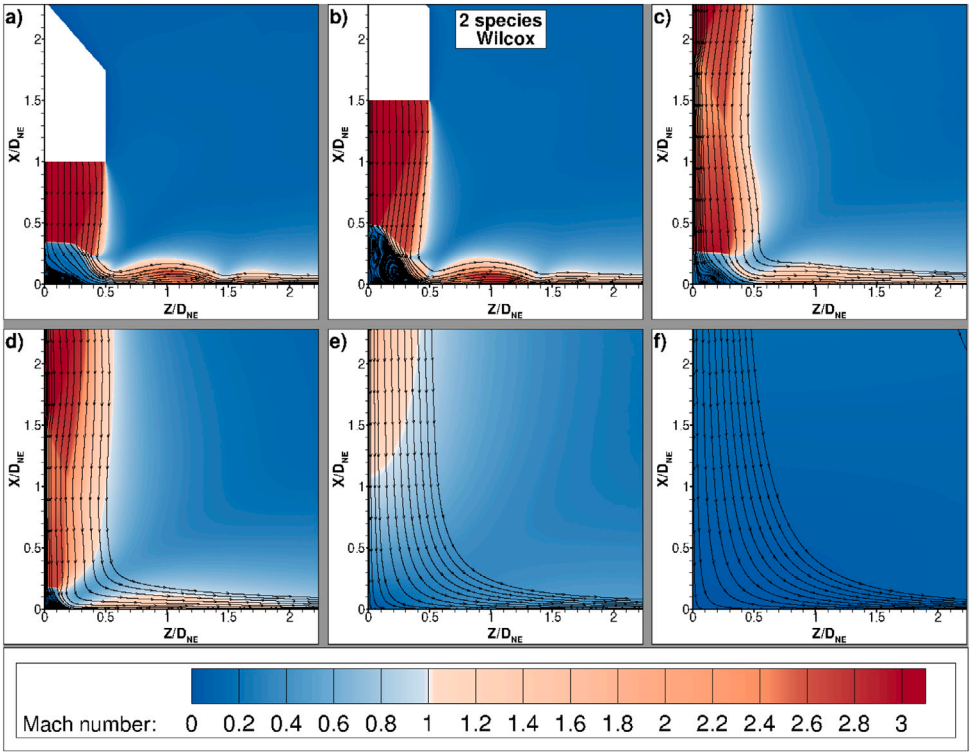

Fig. 28. Plume ground interaction simulations for different nozzle to ground distances [48].

by plume effects [39]. As a result, the freestream stagnation temperature is less relevant and is not critical for an aerodynamic appraisal of a re-usable booster. Simulating the aerothermal effects due to the plume are decribed in more detail in Section 4.2.

For subsonic testing, experiments look to replicate the conditions during the landing burn. This phase of flight lasts approximately 20 s and commences at low altitudes. This means that the freestream conditions experienced in flight are very similar to those which can be replicated in a subsonic wind tunnel located at or around sea level. The centre engine on the Falcon 9 is ignited at a Mach number of approximately 0.75 and is cut at touchdown when the vehicle is stationary. The investigation of subsonic landing burns between Mach 0.75 and 0 is typical for experimental campaigns which have been conducted to date, such as those presented by Marwege et al. [46], where an open jet facility with a subsonic nozzle was utilised. It is also possible to investigate these types of flows using existing facilities developed for aircraft applications [14,113,114]. These tunnels are of the closed or "Göttingen" type, where a constantly running fan provides unlimited test times.

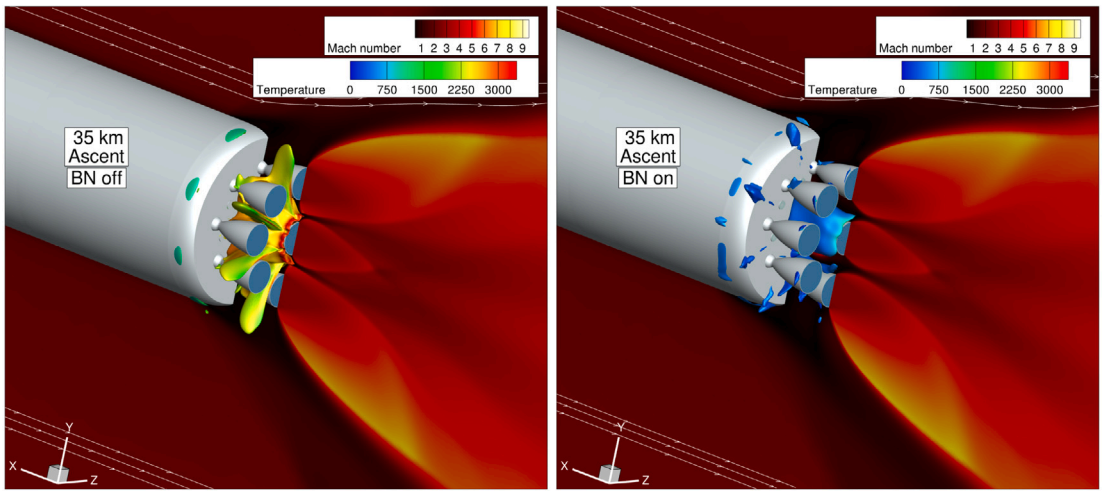

Fig. 29. Comparison of flow field for 9 engine ascent without (BN off) and with (BN on) secondary nozzle. $u = -200\,\mathrm{m\,s^{-1}}$ iso-contour textured with temperature to indicate back flow [111].

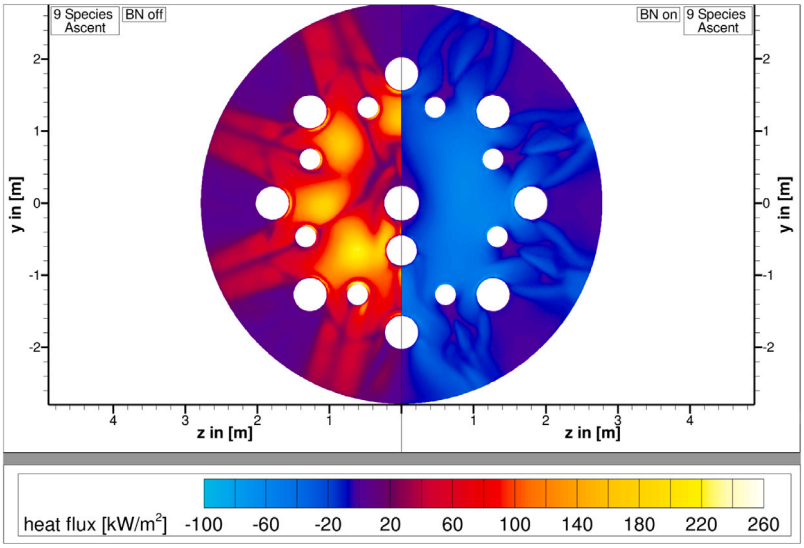

Fig. 30. Comparison of baseplate heat flux for 9 engine ascent without (BN off) and with (BN on) secondary nozzle. Wall temperature $T_W = 600\,\mathrm{K}$. [111].

Facility selection for a retro-propulsion campaign is however not solely dependent on the test time, test section dimensions and achievable freestream Mach number. The availability of infrastructure allowing plume simulation is critical. A brief overview of the design considerations surrounding hardware requirements within the context of similarity parameters is covered in Section 4.2. Finally, thought must be given to fore and aft placement of the model within the test chamber, as well as blockage associated with the retro-plume [100]. Historically blockage is calculated using model frontal area, however for retro-propulsion applications, blockage calculations should be performed based on the largest value of either the model frontal area or expected frontal area of the plume [100]. Concerns relating to wind tunnel flow disturbances and unstart due to the presence of the retro-plume have also been discussed in the literature [100,113,115,116].

4.2. Critical similarity parameters

In an ideal world, experiments would be able to perfectly match flight conditions, allowing engineers to modify their designs according to measured values which will be truly representative of the thermal and aerodynamic loads experienced by the vehicle. Unfortunately, this is not possible due to limitations placed on ground based facilities, including but no limited to, model scale based on test section dimensions, achievable flow conditions in the test section, or safety constraints governing the use of combustible fuels. This then puts an emphasis on key criteria, which are used to evaluate the closeness of the test environment to expected flight conditions.

For low enthalpy flows (less than 2 MJ/kg), which are experienced during the return to earth flight of a booster, perfect gas assumptions are a good approximation. This means that from a facility selection and model sizing point of view, the key parameters to be considered are the Mach and Reynolds number [117]. The Mach number signifies the ratio of flow velocity to the speed of sound in a gas, crucial for simulating inviscid similarity. Meanwhile, the Reynolds number describes the ratio of inertial and viscous forces in a flow; lower values imply laminar behaviour while higher values denote turbulence. Achieving Reynolds number similarity between flight and experimentation is crucial for accurately reproducing viscous phenomena such as laminar to turbulent transition. However, achieving this in a wind tunnel setting is often impractical due to constraints on model size imposed by test section dimensions, limits from instrumentation and mounting infrastructure. These constraints, in turn, restrict the achievable Reynolds number, which is contingent upon the characteristic length of the model. Over

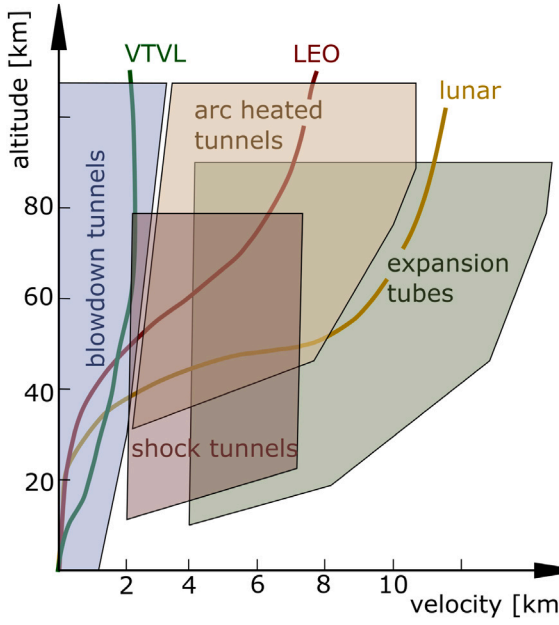

Fig. 31. Applicable facilities for hypersonic phases of flight with overlaid trajectories. *Source:* Adapted from [71].

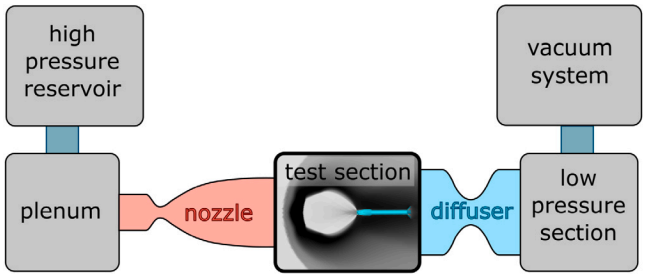

Fig. 32. Schematic of a blow down hypersonic wind tunnel. *Source:* Adapted from [71].

time, aerodynamicists have devised various strategies to address these issues and adjust the achievable Reynolds number to better reflect flight conditions. These strategies include boundary layer trips [118], altering the facility's working fluid [119], or implementing pressurised wind tunnels to isolate Reynolds number effects for a given Mach number by introducing density variations to the flow [120]. The cryogenic wind tunnel was also developed as a means to increase Reynolds number without excessively enlarging the wind tunnel or raising operating pressure [121].

While Mach and Reynolds number similarity are important parameters, for retro-propulsion tests, it is critical that the shape and structure of the plume under flight conditions can be reproduced in sub-scale experiments. This is typically quantified by the radial expansion of the plume, as well as the jet penetration length and the resulting shock stand off distance. Even with the presence of a retro-plume, the flow field in the base region has been shown to be dependent on the vehicle geometry, which necessitates geometric similitude between flight vehicle and scale models used for wind tunnel tests [122]. For the plume itself, as mentioned in Section 3.1, there are short and long penetration modes which are observed in retro-propulsion flow fields. Replicating the penetration length in hypersonic and supersonic retro-propulsion cases has been shown to be dependent on the thrust coefficient as presented in Eq. (1), there T, q_∞ and A_B denote thrust, dynamic pressure and the base area of the rocket respectively.

$$C_T = \frac{T}{q_\infty A_B} \tag{1}$$

The conditions for switching between long and short penetration modes remain debated, with key factors including the exit-to-ambient pressure ratio, thrust coefficient and EPR. While some theories link the switch to changes from underexpanded to overexpanded conditions, it is generally agreed that the switch between blunt and long penetration modes occurs at low thrust coefficients [9,10,100,122,123]. The thrust coefficient takes the exhaust gas properties, as well and the vehicle geometry and freestream conditions into consideration. The ratio of specific heat in the exhaust therefore plays a role in the plume structure. It is essential to consider that a typical rocket plume of exhaust gases will have a ratio of specific heats around 1.2. This is significantly lower than the inert gases which are selected for plume simulation (air at 1.4 and helium at 1.67). Jarvinen et al. [10] discusses that to account for this deviation, adjustments are necessary to accommodate variations in flow turning angle with pressure ratio. This can be achieved by assessing the sensitivity of vehicle and model exhaust gas pressure with respect to flow direction. A curve overlay procedure determines the optimal model exit Mach number which accounts for the variation in ratio of specific heats. The plume sensitivity to the ratio of specific heats is well illustrated by Vos et al. [33], where both plume penetration length and radial spreading are affected as shown in Fig. 33

For subsonic testing, the plume length is reliant upon the square root of the momentum flux ratio (MFR) [11], as governed by Eq. (2).

$$MFR = \frac{\rho_e u_e^2}{\rho_\infty u_\infty^2} \tag{2}$$

The degree of plume expansion and jet structure at the nozzle exit can be replicated by considering the ambient pressure ratio [35]. This is the ratio of the nozzle exit pressure to the ambient pressure in the freestream. This relationship, known as the ambient pressure ratio (APR), is shown in Eq. (3).

$$APR = \frac{P_e}{P_a} \tag{3}$$

For hypersonic Mach numbers, it has been shown that the APR is not a suitable parameter to describe retro-propulsion flow field similarity. This is because it suggests that the expansion of the plume is highly dependent on the freestream Mach number, which is not the case [100]. It has been suggested that the APR be modified to the EPR, which is instead a ratio of the nozzle exit pressure to dead air pressure. The EPR is therefore a more accurate similarity parameter, because the local base pressure is where the plume is actually expanding into. However, because the dead air pressure cannot be calculated analytically, this similarity parameter presents difficulties. It has therefore been proposed that simpler methods, such as the use of ratio of nozzle exit pressure and the total pressure behind the normal section of the shock, is a better matching criterion [124].

While achieving similarity for these parameters will ensure a plume structure which is representative of a full scale vehicle and is key for aerodynamic analysis, the aerothermal environment cannot be replicated using these criteria alone. For the correct scaling of aerothermal effects, some consideration needs to be given to the principle of energy conservation. This requires replicating the ratio between the product of total temperature and the specific heat of the jet and the freestream as seen in Eq. (4) [122]. This is in essence a total enthalpy ratio (TER).

$$\mathrm{TER} = \frac{C_{p,j} T_{T,j}}{C_{p,\infty} T_{T,\infty}} \tag{4}$$

As has been discussed previously, the total temperature of the flow cannot be completely matched in low enthalpy facilities. However, as this term is lower than for flight scales and is in the denominator, it can help to inflate the ratio. The numerator is however the problematic area, as the total temperature of the flow at the nozzle exit for a flight representative engine is typically up to around 4000 K [69]. This makes attempts to replicate the aerothermal environment with a cold air plume futile and mandates the use of high temperature plumes if representative thermal loads are to be measured.

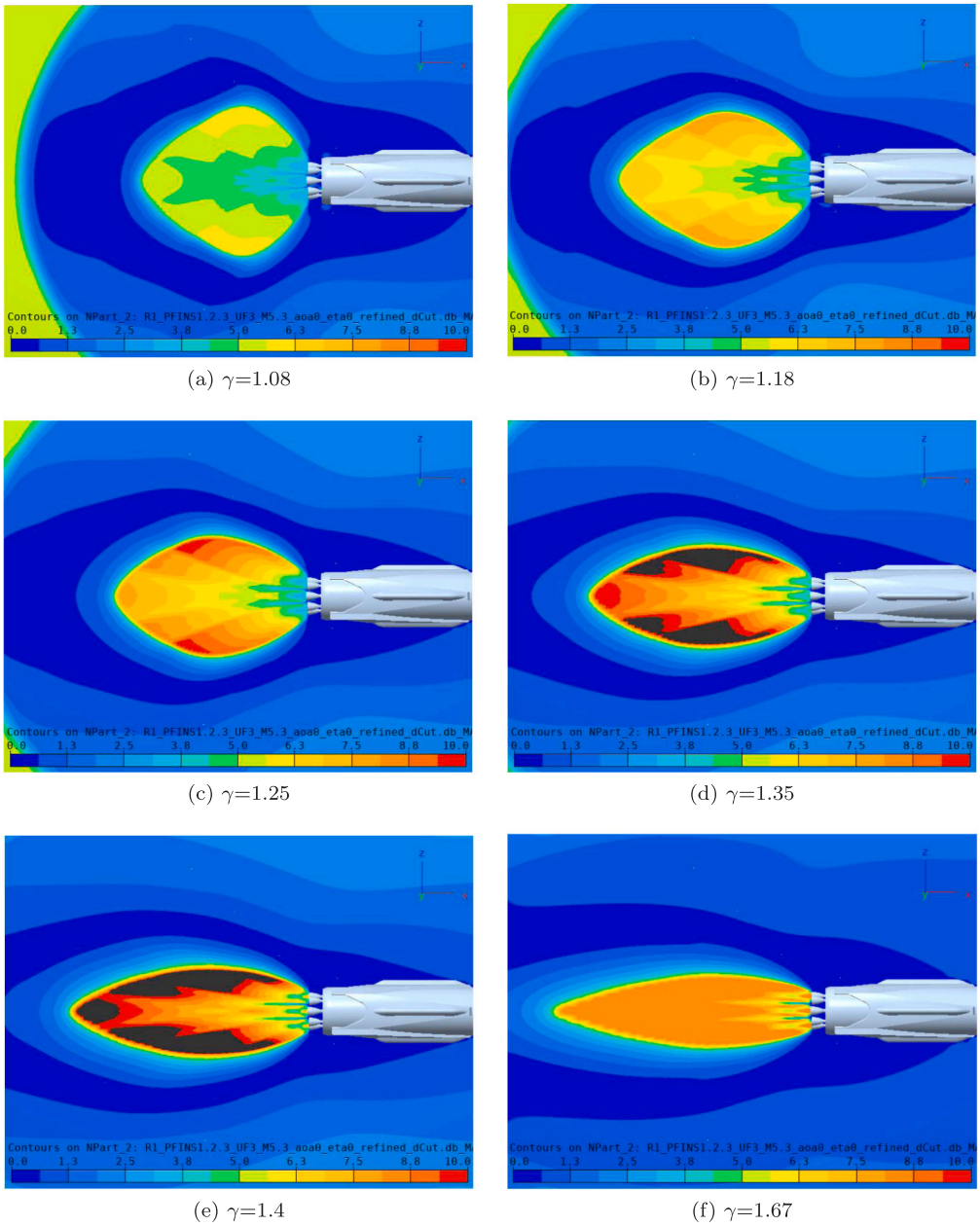

(a) γ=1.08 (b) γ=1.18

(c) γ=1.25 (d) γ=1.35

(e) γ=1.4 (f) γ=1.67

Fig. 33. Sensitivity of plume to variations in ratio of specific heats [33].

4.3. Model design

The design of the model is heavily reliant on the similarity criteria discussed in the previous section. The choice to conduct aerothermal testing with hot plumes is crucial in the early phases of model design, as it determines the need for a thermal mitigation strategy. To match the total enthalpy ratio between experiments and flight, a method for increasing the ratio of exhaust gas enthalpy to the freestream enthalpy is required. There are many potential avenues to explore to achieve this, including heated air [36] or using a fuel and oxidiser mixture with a combustion chamber [46]. For the latter, consideration needs to be given to the oxidiser-to-fuel ratio (O/F), where low values will keep the combustion chamber temperature low, but will result in significant excess fuel being ejected from the nozzle [43,46]. High temperatures in the stagnation region where the jet gases meet the counterflow have been shown to cause post-combustion and significant heat release [43, 46], which can cause heating on the outer surfaces of the model. The post combustion is visualised numerically in Fig. 34, where CFD computations were completed in support of the subsonic aerothermal tests conducted within the RETPRO project. On the other hand, higher O/F ratios result in high combustion chamber temperatures, shifting the requirement of cooling strategy to the inside of the model [46].

The nozzle contour and expansion ratio is also reliant on the gas chosen for the plume simulation. This relates directly back to the thrust coefficient, where the thrust is calculated based on the area at the exit plane of the nozzle, as well as the exit pressure, ratio of specific heats and Mach number. The difference in ratio of specific heats for different exhaust gases should be considered when designing the nozzle. These differences can arise due to temperature variations from combustion or the use of other gases such as helium [10]. Additionally, the temperature at the nozzle exit plays an important role if using air for plume modelling. The condensation issue which was described previously for blow down tunnel facilities can also present itself, where flow expansion through the model nozzle can lead to condensation within the plume. This is a topic which has been investigated in detail [41,100], where it was shown that condensation is often present

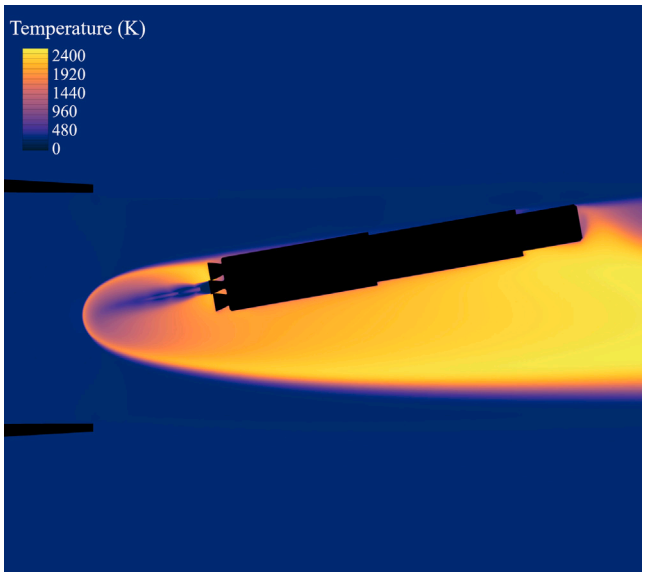

Fig. 34. High temperatures due to post combustion identified during CFD studies (O/F=0.471).

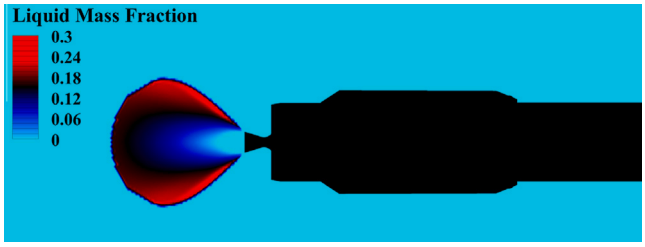

Fig. 35. Predicted condensation using equilibrium condensation model [44].

in cases where the air is not heated, but its influence on plume structure and the aerodynamic loads are minimal [44]. Fig. 35 presents a CFD solution using an equilibrium assumption, thus portraying a worst case scenario for possible condensation during experiments representative of a single engine re-entry burn conducted using unheated air.

As with most small scale wind tunnel models, it is generally preferred that the size is as large as possible to inflate Reynolds number and maximise internal space for easy integration of instrumentation and mounting infrastructure. Larger model scales are particularly useful for retro-propulsion cases where manufacturability of components is extremely challenging on small scales. Nozzle throat diameters in the range of 5 to 8 mm have been reported in the literature, where 3D printing technology has been utilised to manufacture nozzle pieces [98,114]. Fabrication of small parts is not limited to nozzles, with successful examples of miniature grid fins being manufactured and wind tunnel tested within the RETPRO project [41]. Despite the advantages associated with increasing model size to account for these intricate components, there does exist an upper limit for model size, which can either be determined by restrictions stemming from the wind tunnel nozzle or test section blockage. Shortened models have been used in some test campaigns to ensure the plume and model remain inside the undisturbed core flow region of the freestream [41]. Additionally, wind tunnel blockage during retro-propulsion tests, which is no longer purely a factor of model frontal area, can play a role in selected nozzle expansion ratios and model diameter [100]. Analytical methods for the prediction of plume shape do exist and are discussed in Section 5.1, which can be used to estimate blockage, however it is more frequently seen that such an analysis is conducted using CFD [100]. This is because other phenomena may be present which can influence the model design

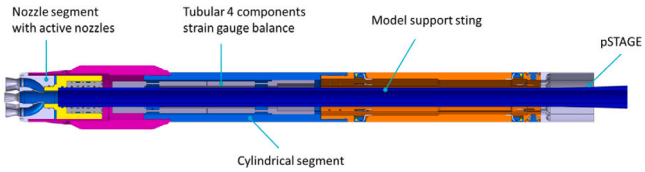

Fig. 36. Example of added wind tunnel model complexity with internal flowpath servicing multiple nozzles and load cell integration [36].

or placement. Examples of this include plume size and shape variation with freestream conditions or thrust coefficient [100]. Static conditions in the test chamber of some facilities can also vary over time due to the accumulation of gas, arising from the inflow of the freestream and mass flow from the retro-plume [98]. For this reason it is advantageous to have a CFD campaign prior to the experiments to help guide the experimental setup and understand potential design issues in advance [100]. An added advantage of this approach is the the grid and setup can be used for numerical rebuilding of the tunnel tests for validation purposes [42,100].

The challenges associated with instrumentation integration are made more difficult due to the presence of an internal flowpath, which feeds the nozzles for plume simulation. This specifically relates to the use of internal load cells or wiring for pressure sensors or thermocouples. These challenges are not only limited to boosters, but apply to all models which are utilised for retro-propulsion tests [14]. Fig. 36 highlights complexity of constructing a subscale model with an internal flowpath. Model support systems need to be modified to allow the flow of exhaust gases to the model [14,36,98,114].

5. Numerical simulations

5.1. Tool applicability, general challenges and problems

Hypersonic gliders or other unpropelled vehicles can use fast, low fidelity tools such as surface inclination methods, as well as empirical relations for surface pressures and stagnation heat flux. Well known examples are the Newton, shock expansion, linearised Euler or potential flow methods [125–130]. This is possible because the freestream conditions are stable and well defined. For supersonic flows, the aerodynamic forces are primarily generated on the pressure side of the vehicle which coincides well with the validity boundaries of those models. In contrast, the effective free stream for a vehicle completing a retro-propulsion burn is extremely complex and cannot be described with simple methods. The plume is projected ahead of the vehicle, meaning the fuselage is subjected to an unsteady, exhaust gas rich flow field. The plume size itself is sensitive to the ambient conditions in the vicinity of the base, which are in turn affected by complex interactions between plume and free stream. In addition, factors such as post combustion and exhaust/air mixing may significantly affect the flow structure. This presents a significant challenge to those wishing to derive analytical solutions to retro-propulsion problems. There have been attempts to mathematically describe the location of key flow features of a retro-propulsion jet, which began with predictions for the location of bow shock, flow interface and the terminal shock for a single jet encountering a Mach 2.5 counter-flow [5], with good agreement observed between analytical solution and experiments. Similar work was conducted for a range of freestream Mach numbers by Jarvinen et al. [10], where a computer program was developed to predict the same flow field characteristics with an error of approximately 10%. Multi-engine plumes were examined by Cordell and Braun [131], with favourable correlations observed between CFD simulations and the developed model. A method to investigate the influence of the plume on the aerodynamic characteristics of a vehicle has also been proposed, where aerodynamic and propulsive interactions are accounted for [132].

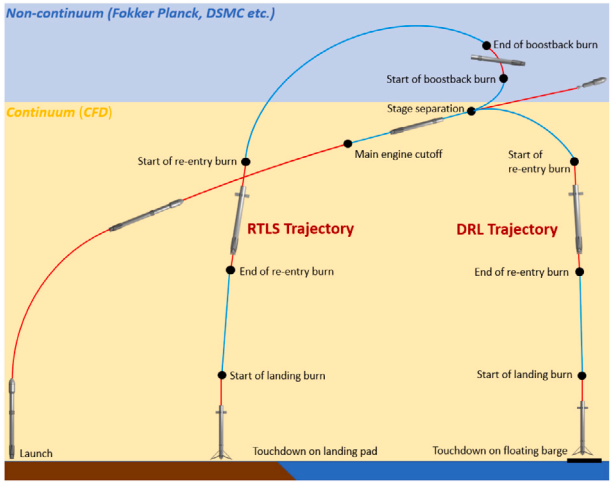

Fig. 37. Overlay of continuum/non-continuum applicability range with Falcon 9 trajectory.

One major drawback of even the most advanced analytical approaches to retro-plume modelling is the inability to predict aerothermal loads or the influence of the plume on downstream aerodynamic control surfaces. As a result, steady state CFD computations based on the RANS to model the turbulent flow appears to be the cheapest and most robust way to generate thermal load data as well as fully characterise the vehicle aerodynamics. However, as shown later in this chapter, RANS based turbulence modelling is one of the primary sources of uncertainty specifically for the prediction of thermal loads. This is because of the complexity of the highly compressible flow field and the occurrence of a large variety of gas-dynamic and fluid mechanical phenomena which challenge the applicability of RANS models. Hence, more elaborate scale resolving techniques are required to assess and improve the predictive capabilities of simulation tools particularly for the propulsive flight phases. Besides the turbulence, the other major source of uncertainty is related to chemistry and post-combustion modelling. Especially for hydrocarbon fuels, complex chemical interaction of the exhaust with the ambient air occurs. This can lead to additional heat release close the vehicle surface or impact the plume structure due to endothermal reactions in the hot stagnation region.

Being based on the solution of the Navier–Stokes equations, the use of CFD is strictly only valid in the continuum regime. This means that manoeuvres such as the boost-back burn may not be accurately evaluated. However, as shown in Fig. 37, the key phases of re-entry, aerodynamic glide as well as the landing burn can be covered by Navier–Stokes solvers. Further, even at higher altitudes, Navier–Stokes can still be applied to the near field in the vicinity of the rocket base which is governed by the continuum flow of the exhaust plumes. The modelling of large scale plume structures which are in the continuum regime further presents a major challenge for the application of dedicated methods for rarefied flow such as Direct Simulation Monte-Carlo (DSMC).

Generally, CFD techniques require a set of sub-models and methods which can be grouped into (1) discretisation and solution schemes to consistently transfer the governing partial differential equations into an algebraic system and solve it; (2) models to account for the effects of turbulence; (3) models for viscous transport phenomena such as mass and heat diffusion; (4) models for the thermodynamic and transport properties of the participating gases, and, (5) models for post-combustion and chemical reactions. Each of these sub-models impose significant difficulties due to the complex physics of the compressible high speed and high enthalpy reacting flow environment during the retro burn phase. Some of these aspects are discussed in the following subsections.

5.2. Discretisation schemes and solution techniques

Today, by far the most widely used schemes are finite volume (FV) methods. The idea is to use flux functions to compute mass, momentum and energy fluxes across cell boundaries and construct the iterative cell update (residual) from their balance. FV methods are based on the integral formulation for the applicable conservation laws and are therefore particularly attractive for Navier Stokes equations in the presence of discontinuities such as shocks. The inviscid fluxes are computed from reconstructed states at both sides of the cell boundaries. This reconstruction scheme uses available cell averages and determines the order of accuracy of the numerical method. Slope limiters are used to limit gradients during the reconstruction process to stabilise the solution around discontinuities and in regions of steep gradients with associated local extrema. This adds additional numerical dissipation in critical regions. The fluxes across the cell boundaries are then computed from the states at both sides of the cell boundaries by approximate Riemann solvers. This approach captures the hyperbolic characteristics of Euler equations at Mach numbers above 1 and thus avoids non-physical upstream propagation of disturbances.

This means that numerical simulation of supersonic flows with discontinuities (shock waves) imposes conflicting demands on the formulation of numerical solution scheme. It needs to provide sufficient dissipation to capture strong shocks without developing instabilities and oscillations in the vicinity of the discontinuity. Nevertheless, the numerical dissipation has to be much smaller than the physical viscosity to accurately compute boundary and shear layers. The simultaneous satisfaction of these two requirements makes the computation of complex supersonic flow fields as present in retro-propulsion extremely challenging. Further, FV methods capture shock waves in numerical control volumes which results in an alignment of the shock with the computational grid. The resulting distorted shock shape often produces nonphysical downstream noise and disturbances [133]. Further, strong shock waves can produce large errors when the shock is not aligned with the grid. A well-known example is accumulation of errors in the stagnation region of a blunt body downstream of the strong bow shock which leads to a complete breakdown of the numerical solution and meaningless results (carbuncle phenomenon) [134].

Particular challenges are related to the construction of the spatial discretisation or computational grids on which the equations are solved. Flow fields are characterised by the presence of very large gradients. For example, the accurate representation of temperature gradients close to the wall which is required for heat load prediction leads to the requirement of a very tight wall normal grid spacing [135] in the order of 10^{-6} m which also results in unfavourable large cell aspect ratios above 10^4. Generally, the generation of meshes can be complex, especially if the vehicle utilises intricate control surfaces such as grid fins (see Fig. 38). In these cases the number of grid points required to capture the geometry and the complex flow features inside the cells of the grid fin can become very large. Often, the accurate prediction of parameters which can influence the aerodynamic coefficients, such as mass flow through grid fin cells or shock location is heavily dependent on the grid resolution in these areas. This applies especially to the critical flow conditions around the choking limit of the grid fin.

5.3. Turbulence

Turbulence is one of the last subjects of classical physics which is still not solved. Hence, practical simulations need to rely on approximate turbulence models. The most common approach is to consider the Reynolds or Favre averaged Navier–Stokes equations. These are based on a time or ensemble average of the turbulent fluctuating quantities in the governing equations. Thus the idea is rather than aiming for instantaneous time resolved turbulent flow field, averaged mean numerical solutions are obtained on comparatively coarse grids

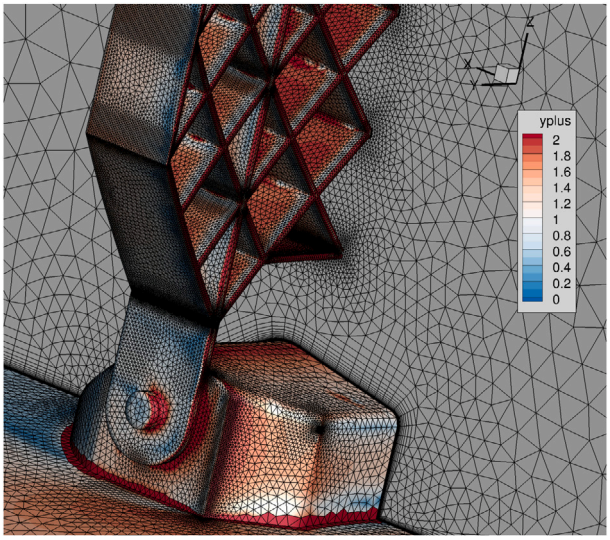

Fig. 38. Example of grid complexity for grid fins [110].

without the requirement to resolve turbulent structures. Due to the non-linearity of the Navier–Stokes equations, the averaged equations are not closed. Instead, additional terms appear which express the mean macroscopic effects of turbulence for momentum, mass and energy transport. These terms contain correlations of the fluctuating part of the variables and cannot be evaluated directly. The modelling of these terms using only known mean flow properties is the task of turbulence modelling.

For momentum transport, the unclosed correlation terms can be grouped in a tensor of apparent turbulent stresses called Reynolds stress tensor. Eddy viscosity models use Boussinesq's hypothesis to model this stress tensor using a scalar eddy viscosity assuming a linear relationship with the strain rate tensor. This scalar is usually computed from a semi-empirical set of transport equations. The most popular two-equation models use one equation a quantity which characterises the turbulent kinetic energy and one equation for a turbulent length scale or dissipation rate. Validity concerns for Boussinesq's hypothesis exist even for simple flow fields [136] and a more physical representation of the Reynolds stress tensor is still an active area of research. This leads e.g. to the development of non-local models [137] or Reynolds Stress models (RSM) [138] which provide an improved solution accuracy at only moderately increased computational cost. Being initially developed for incompressible applications, the application of RANS turbulence models to highly compressible flow is justified by Morkovin's hypothesis which results in the fact that compressibility effects can be accounted for by scaling of the turbulent quantities with the mean density [139]. However, there are concerns about its applicability for flows with large compressibility, temperature or density gradients. Indeed, standard RANS turbulence models do not predict the experimentally observed reduction of the shear layer or jet spreading rate at large Mach numbers. This drawback can be fixed by introducing compressibility corrections as proposed for example by Sarkar [140], Zeman [141] or Wilcox [139]. However, it has to be noted that these compressibility corrections are now believed to be grounded in incorrect physical assumptions [142]. Nevertheless, they reproduce the observed spreading rates. Large density variations between jet and outer flow (above a ratio of two) tend to increase the spreading rate of a turbulent mixing layer [143,144]. This effect is generally under-predicted by RANS models but yet highly relevant for retro-plumes.

Another problem is the inability of some models (e.g. $k-\epsilon$) to predict the spreading rate of round jets, which is known as a round-jet/plane-jet anomaly [139] and corrective approaches need to be considered. An assessment of popular models to address the round jet anomaly is given by Davidenko et al. [145].

A general and systematic deficiency of current turbulence models, which are based on the RANS, is their inability to correctly predict the interaction of turbulence with shocks. This is because RANS models do not account for the unsteady motion or fragmentation of the shock wave within the interaction zone [146]. Typically, significant over-prediction of the turbulent energy amplification occurs without dedicated adjustment of the applied turbulence model [147].

The modelling of turbulent heat and mass transport phenomena relies on assumptions for the turbulent Prandtl and Schmidt numbers, respectively. These numbers are used to estimate an apparent heat conductivity and diffusion coefficient from the modelled eddy viscosity and their values for complex mixtures is highly uncertain. Several semi-predictive approaches exist. They mainly rely on the solution of additional transport equations for the fluctuation intensity of the temperature or internal energy and species concentrations [148,149]. Results from this approach and more fundamental DNS studies [150] suggest ranges for turbulent Prandtl and Schmidt number between 0.3 and 1.0 observed in shear layers with large density and temperature gradients. Hence, the modelling of turbulent diffusion processes in a RANS framework is still associated to large uncertainties.

Examples to highlight the uncertainty from RANS turbulence modelling in practical applications are shown in Figs. 40, 41, 42 and 43. A comparison of LES and RANS results for a supersonic retroplume exhausted by a Falcon 9, based on the single equation Spalart–Allmaras (SA) model, were presented by Ecker et al. [24]. The results for a representative trajectory point are shown in Fig. 40. While both modelling approaches show a large detached shock wave upstream of the vehicle and the supersonic exhaust plume, significant smearing out of the shock wave due to large scale plume unsteadiness in the LES is present. The plume isosurface itself appears similar in shape and distribution however an increase in flow temperature, which further penetrates laterally into the farfield, is shown for the LES case. The vehicle surface gas temperature distribution for both RANS and LES are presented for the surface envelope and mean in Fig. 41. The RANS results show a larger range of values in the envelope, most likely due to the lower interaction with the lateral farfield. Averaged along the radius the mean values are similar for LES and RANS, thus making even one equation RANS a viable approach for loads estimation especially in the early design stages and supersonic retropropulsion phases. From a purely aerodynamics point of view, the plume shape and the resulting recirculation zones which form on the leeside of the plume play a large role in determining the surface pressures on the vehicle. The influence of modelling approach can be seen in Fig. 39, where pressure coefficient data from LES and RANS simulations are compared with experimental data for a variety of surface pressure tap locations. In some cases the wind tunnel pressure results are closer to the RANS calculations, while at other times the LES gives a better comparison [151].

Fig. 42 compares heat flux predictions from different popular eddy-viscosity models (Spalart–Allmaras, Wilcox k-omega and Menter Shear Stress Transport (SST)) during a retro-burn at supersonic speeds. Whereas the shape and size of the plume, particularly its radial boundary, is only slightly affected, the heat flux on the fuselage differs by a factor of 2 between the one-equation Spalart–Allmaras and the two-equation Menter-SST and Wilcox k-omega models.

Fig. 43 shows different plume shapes during a subsonic landing burn manoeuvre, again resulting from the application of different RANS turbulence models. Dramatic differences can be observed for the plume length, radial extent and the structure of the recirculation zone.

In summary, RANS models suffer from very significant modelling uncertainties when applied to the numerical simulation of retro-propulsion problems. The plume shape is dependent on turbulence model, particularly at low speed landing conditions. Supersonic retro-propulsion at low ambient pressures appears to be more robust as the plume shape is strongly governed by gas dynamic phenomena

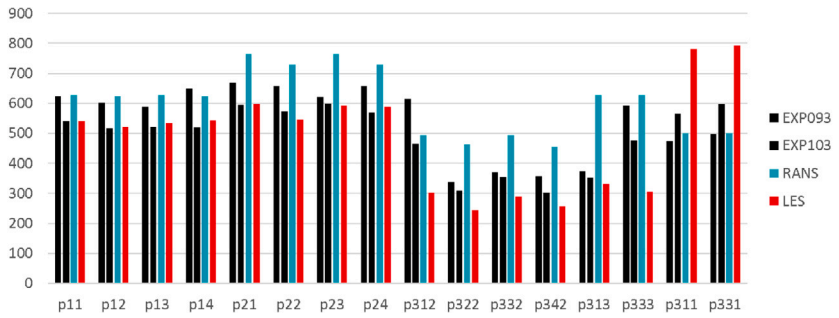

Fig. 39. Comparison of surface pressures for the RETALT vehicle for RANS, LES and experimental datasets [152].

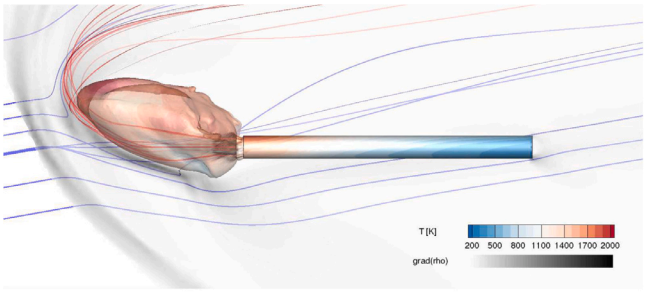

(a) Averaged LES flow field

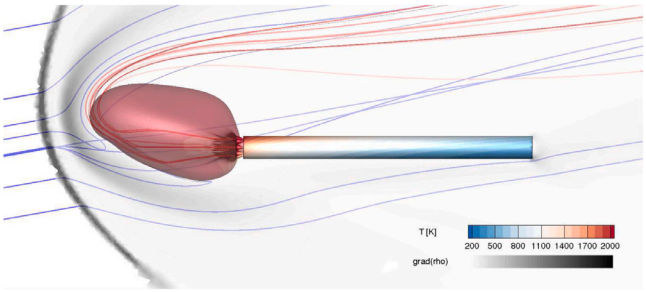

(b) RANS flow field

Fig. 40. Comparison of averaged LES and RANS flow field [24]. Plume is shown as iso-surface at 50% exhaust gas mass fraction. Rocket casing and plume isosurface shows gas temperature contour.

and less by the turbulent state of the shear layers. The recirculation regions which develop between the plume and the vehicle are also sensitive to the turbulence model. A particular challenge for multi-nozzle configurations are strong oscillations between short and long penetration modes of the plume. This phenomenon cannot be captured by steady state RANS simulations. Also unsteady RANS (URANS) approaches are found to not capture this effect. Probably the most significant uncertainties are observed in the predicted surface heat loads. However, RANS models seem to be well suited to predict the surface pressures and aerodynamic coefficients. Due to their low CPU requirements, RANS models are the only option for comprehensive parametric studies during vehicle design and development.

A major step towards more predictive simulation capabilities is the application of scale resolved models such as LES. They require significantly less modelling assumptions and thus provide an increased accuracy. LES techniques rely on a decomposition of the aerodynamic field between the large and small scales of the flow, the largest ones being directly resolved, while the effect of the small ones is represented through the use of a subscale model. This is useful because due to their much more homogeneous, isotropic and self-similar nature, the small scales are considerably easier to model. The production of turbulence through the interaction of the large scales with shear in the mean flow and potential anisotropic properties of the large scales are directly resolved. The computational time scales with the Reynolds number, Re as $t \propto Re^{2.5}$. This is due to the increasing range of size of the turbulent eddies which need to be resolved. Hence, unfortunately, those methods suffer from extreme computational cost for large Reynolds numbers. To remedy this problem, hybrid models are developed which principally aim at modelling the near-wall region rather than resolving it. The most popular approaches are the detached eddy simulation (DES) and wall modelled LES. In DES, a statistical RANS model is used in the boundary layer and wall modelled LES relies on the application of local wall models which exploit self-similarities in turbulent boundary layer profiles. Here, the computational time scales approximately as $t \propto Re^{0.5}$. However, compared to a RANS simulation the computational cost of a DES is still about a factor of 100 higher which makes this methods unsuitable for the exploration of a large design space. Their use is primarily focused on accuracy assessment of RANS models and accurate load predictions for the most critical trajectory points.

5.4. Chemistry modelling

As seen in Section 2.2, a re-usable first stage enters the atmosphere with significantly less velocity than a space vehicle starting from orbital velocity. Pure aerodynamic heating hence results in the molecules experiencing vibrational excitation as well as very limited oxygen dissociation and Nitric Oxide (NO) formation. However, once the engines are ignited during a retro-propulsion burn, the booster flies through high temperature, fuel rich exhaust gases, which introduces a flow field with significant chemical activity. The peak temperatures are reached in the stagnation zone between the plume and the free stream. Here, the exhaust is stagnated and approximately reaches the combustion temperature when it meets the incoming air which is heated by the bow shock formed at the upstream end of the interaction zone.

Assumptions relating to the species behaviour in the flow need to be made and can play an important role in balancing accuracy and computational cost of a simulation. One such assumption is that the flow is in chemical equilibrium, which operates under the premise that the chemical reactions occur rapidly compared to the time the fluid takes to move through the flow field. In reality, this assumption implies infinite chemical rates and is therefore a hypothetical case. On the other end of the spectrum is the assumption of frozen chemistry, where no reactions are taking place in the flow and the mass fractions of the species are fixed. Finally, nonequilibrium flow acknowledges that chemical reactions and other processes do not occur instantaneously and that there are chemical reactions, which have not reached equilibrium, occurring as the fluid element travels along a streamline. Numerically this introduces a large added computational cost due to the necessity to solve additional species continuity equations, and, most importantly, to compute the local production of species due to chemical reactions using finite-rate chemical kinetic mechanisms. Especially for hydrocarbon fuels, these reaction mechanisms can be very complex and mathematically stiff. Also the assumption of chemical equilibrium introduces significant demand on the computational infrastructure because the relative amount of atoms differs in the flow field due to

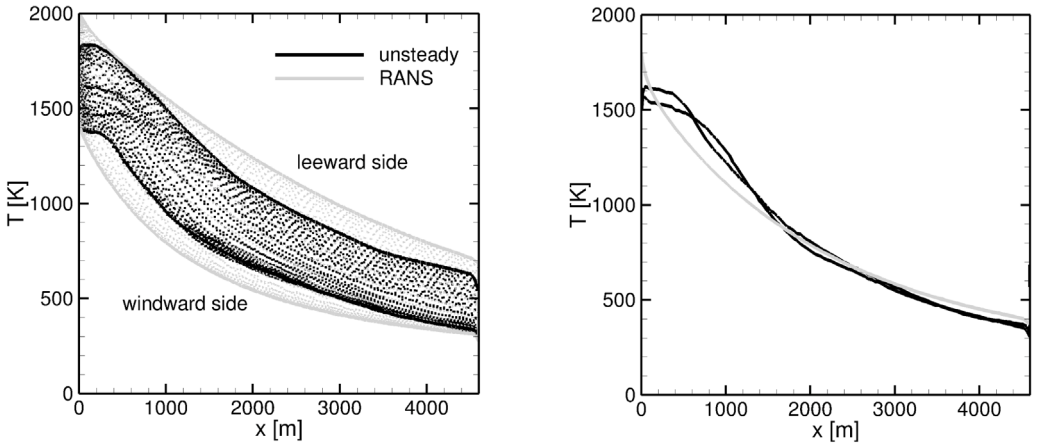

(a) Envelope of surface gas temperature for both averaged LES and RANS calculation.

(b) Mean of surface gas temperature for both averaged LES and RANS calculation.

Fig. 41. Comparison of averaged LES and RANS surface gas temperature [24].

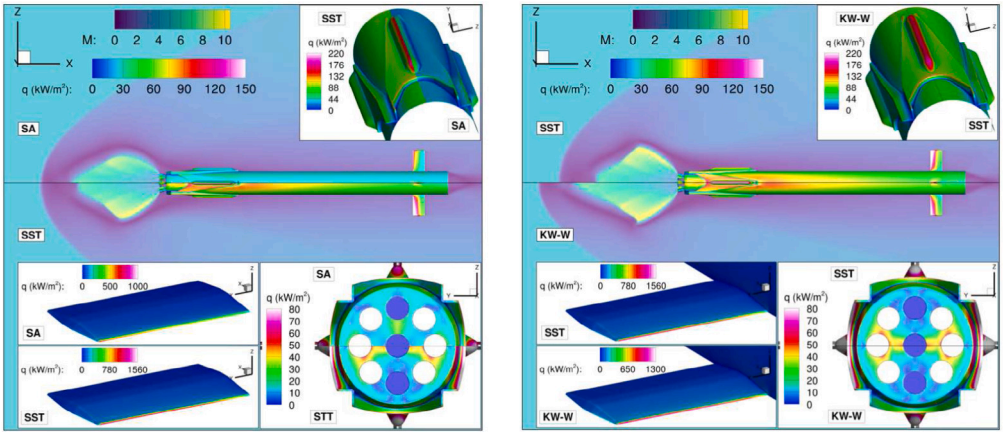

(a) Plume shape and surface heat flux comparison with SST turbulence model

(b) Plume shape and surface heat flux comparison with Wilcox turbulence model

Fig. 42. Comparisons showing plume shape and surface heat flux between different turbulence models for re-entry burn conditions as part of full-scale vehicle CFD simulations within the RETALT Project [39].

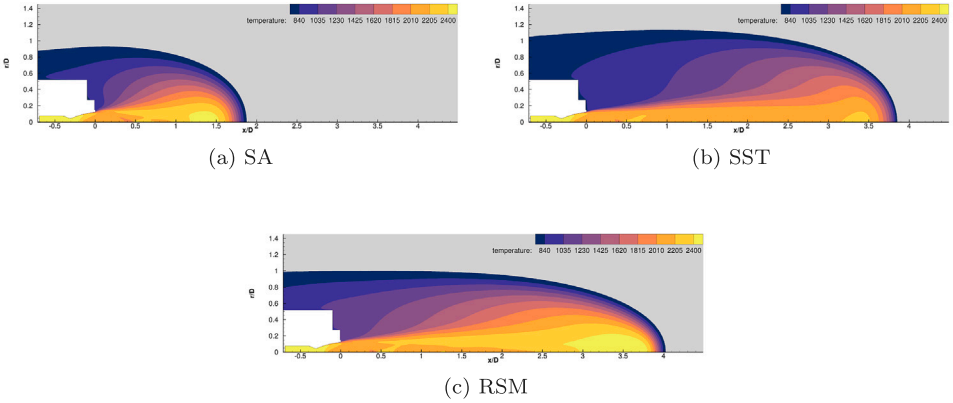

(a) SA

(b) SST

(c) RSM

Fig. 43. Visualisation of plume sensitivity to turbulence model under landing burn conditions for the CALLISTO vehicle [65].

mixing of different exhaust gases with the air. This results in either complex multi-dimensional lookup tables or the need to solve the local equilibrium problem to obtain the local thermodynamic properties of the gas. The chemical regime (equilibrium, non-equilibrium or frozen flow) depends on the ratio of chemical and fluid dynamical time scales which can be expressed in terms of a Damköhler number. If both are comparable and chemical heat release is significant, non-equilibrium modelling is mandatory. The chemical time scale itself strongly depends on the local flow conditions and is generally short for combustion phenomena at high pressures and temperatures. Nevertheless, secondary

effects such as the formation of oxides of nitrogen (NOx) due to the interaction of the exhaust with the ambient air or post combustion at low pressures and temperatures can result in very large chemical time scales which exceed typical fluid dynamical residence times by orders of magnitude. Hence, depending on the specific problem, frozen, equilibrium and non-equilibrium regions can be simultaneously present in a retro-propulsion flow field.

It should be noted that, due to complex scaling laws, the reproduction of chemical kinetics or time scales in ground based test facilities is very difficult if not impossible. The reaction rates scale exponentially with the flow temperature and with the pressure for pressure dependent reactions. The species production (and hence global heat release rates) scale with the reaction rate and the product of density and length scale for two-body reactions or with the product of square density and length scale for three-body reactions (due to the law of mass action). Hence, flow temperature, pressure, density and length scale need to be reproduced for chemical self-similarity and the application of CFD appears to be the only choice to accurately re-produce post combustion and chemical interaction effects at flight conditions.

For non-equilibrium computations, chemical reaction mechanisms are selected based on the species present in atmospheric air and the exhaust gases of the thrust and gas generator nozzles. Detailed mechanisms can include hundreds of species and reactions [153] and introduce large CPU cost and stability issues in the numerical solution. Hence, simplified skeletal or global mechanisms were developed (e.g. [154]) which are valid in a reduced range of temperatures, pressures and mixture fractions and are tuned to specific quantities of interest such as the global heat release. This is supported by the fact that quantities which are relevant for pure combustion modelling like flame speed or ignition delay are not important for retro-propulsion simulations. The latter generally take a more global approach, where the sensitivity of a solution to a kinetic mechanism is generally based on the flow field temperature or global chemical heat release and the resulting surface heat flux.

Computations using a frozen assumption are typically used as a baseline for the evaluation of the influence of a chemically reacting flow field, as a frozen flow is the simplest and computationally cheapest way to model a retro-plume. This is evidenced by the preliminary studies conducted by Laureti et al. [39], where a simple 2D axisymmetric computation was conducted for a hydrogen fuelled rocket performing retro-burns are Mach 5 and Mach 2 at altitudes of 30 km and 15 km respectively. Here the detailed reaction mechanism including 9 species and 19 reactions [155] was compared with a frozen assumption. For both Mach numbers it was found that a frozen chemistry assumption is sufficient for the prediction of surface heat loads, in spite of the fact that a frozen assumption does not account for additional heat release due to post-combustion of the fuel rich exhaust, or heat absorption through processes such as endothermal dissociation. The latter was found to be the principle mechanism behind lower peak plume temperatures seen in the vicinity as shown below in Figs. 44 and 45.

A similar precursor study was conducted in the early stages of the RETPRO project, where both hydrogen and kerosene fuels were investigated during a retro burn occurring at Mach 1.2 and an altitude of approximately 1.5 km. This condition is representative of the beginning of the landing burn. Fig. 46 shows that the same 200 K difference in the near wall temperatures was observed for the test cases for frozen and nonequilibrium chemistry with the hydrogen fuelled rocket, while a significant difference was observed when switching to kerosene. This case showed a more significant impact of chemistry, as evidenced by the approximately 650 K increase in the gas temperature close to the surface. This corresponds to a relative error of 40% when compared to the frozen computations. The simple 3-step global mechanism performed remarkably well with only 50 K difference to the full chemistry and was the basis for selecting the simple mechanism for the detailed 3D computations of the launcher.

The importance of post-combustion effects was further observed for the full RETPRO configuration at the end of the entry burn. At the leading edges of the fins, the authors noted peak fluxes of about 400 kW/m^2 for the reacting case and 350 kW/m^2 for the inert results. The most important impact of post combustion was observed close to the fuselage properly reference Fig. 47(b). In spite of the generally low levels, local increases of surface heat fluxes by about 50% are seen. The heat load distribution on the baseplate was hardly influenced by post-combustion effects as visible in Fig. 47. This is due to the absence of atmospheric oxygen in the exhaust-gas rich flow field in the vicinity of the rocket base.

Concerning general flow field properties, it was observed that the temperature in the stagnation zone between the engine exhaust and the free stream was higher in the frozen case, due to the endothermal reactions from the high stagnation temperatures and the aerothermal heating of the strong bow shock. This effect was compensated further downstream where recombination occurs and the flow temperatures in the vicinity of the rocket vehicle were comparable between the two cases.

In summary, the application of numerical simulation methods to retro-propulsion systems is still associated with significant challenges and uncertainties. These are mainly related to turbulence and chemistry modelling. Limited available validation metrics are mainly based on scaled wind tunnel experiments. They allow an assessment of the accuracy of results for heat loads or the aerodynamic performance but generally do not provide insight into specific deficiencies of the applied models. Here more fundamental research is necessary specifically to decrease the large predictive uncertainties associated with RANS models. This applies e.g. for the prediction of compressible shear layers (or jets) with large temperature or density gradients, turbulent heat and mass diffusion processes of shock-turbulence interaction. Precise chemical reaction mechanisms for hydrocarbon fuels are very complex and require significant CPU time. Simplified global mechanisms are generally very limited in the range of validity and need to be carefully assessed before application. Other phenomena like additional heat loads by radiating soot in the exhaust can presently not be modelled with satisfactory accuracy as predictive models for the particle distribution in the exhaust jets of liquid rocket engines are missing.

6. Outlook and potential research needs

6.1. Numerical validation and uncertainty quantification for aerodynamics and heat flux

Numerical validation and the associated uncertainties is a complex topic. From the purely numerical perspective, uncertainty sources for RANS computations are almost unlimited and can be attributed to grid density, turbulence model, discretisation scheme, gradient reconstructions, or correction factors and limiters imposed to improve stability and convergence behaviour. Moving to higher fidelity methods such as DES or LES should theoretically provide more accurate results, but the practicality of widespread use it still limited due to the added grid requirements and computational expense. These current limitations and future needs for the aerospace sector are well known and documented [156]. Aside from the challenges faced on the numerics side, a fundamental issue is often the lack of flight scale data to use for validation. This can be combated by the use of wind tunnel experiments to generate reference data for both the model surface and flow field. This requires the numericists to perform simulations at scale equivalency of the experimental setup to allow correct validation. While this is a valuable exercise, the degree to which validation can take place is limited by the complexity of the wind tunnel tests. For example, surface heat loads cannot be extracted from tests where a cold gas plume is used. In this specific case, experimental facilities are constantly evolving and improving, with emphasis being placed on the ability to conduct aerothermal testing, which will allow the validation

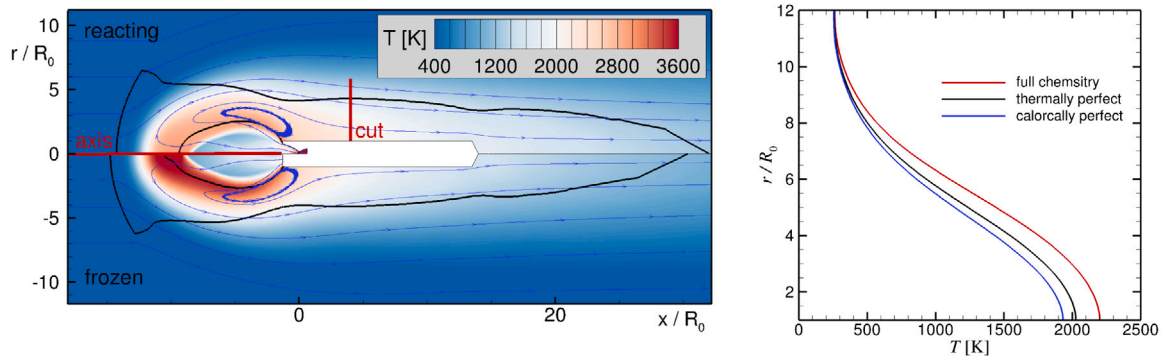

(a) Plume Overview (b) Temperature Profile

Fig. 44. Hydrogen-fuelled rocket completing retro-propulsion burns at 15 km altitude with a Mach 2 counterflow comparing flow field temperature for different chemistry models [39].

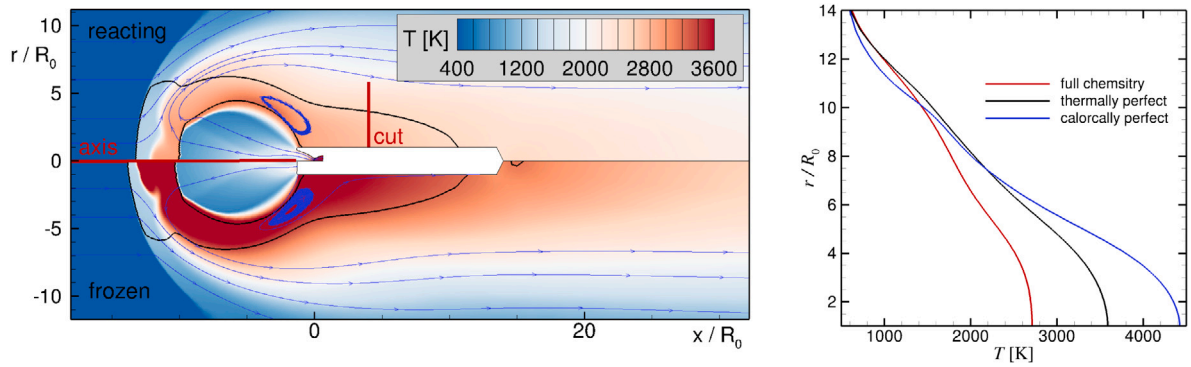

(a) Plume Overview (b) Temperature Profile

Fig. 45. Hydrogen-fuelled rocket completing retro-propulsion burns at 30 km altitude with a Mach 5 comparing flow field temperature for different chemistry models [39].

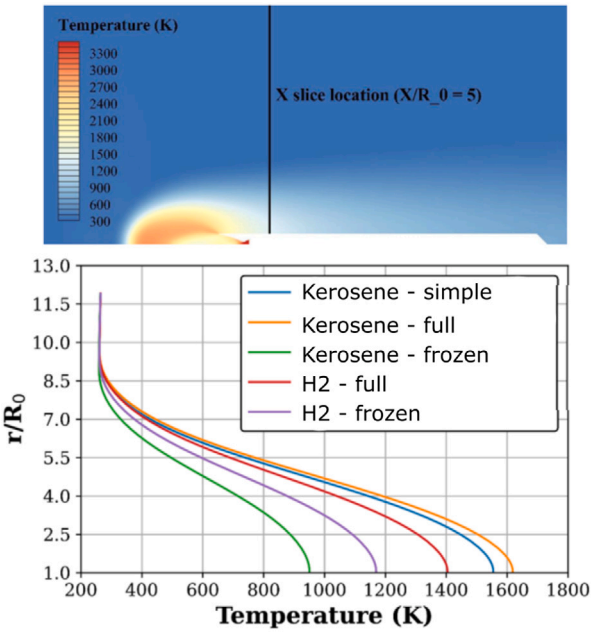

Fig. 46. Evaluation of wall temperature gradient sensitivity to chemistry modelling for kerosene and hydrogen fuelled rockets during landing burn [110].

of thermal loads during a burn [46,157]. The main uncertainty relating to wind tunnel tests is not specific to retropropulsion and is the extrapolation of measured data to flight scales. At present, numerical support is always needed to estimate scale effects where flight tests are not possible. Finally, it must be considered that having high fidelity experimental data specifically for numerical validation is only useful if the simulated result is somewhat similar to what has been measured. In cases where large deviations are observed, the number of numerical uncertainty sources is too high to draw immediate conclusions. In these cases, new experiments would need to be designed to isolate specific physical phenomena such that a build up or, process of elimination type approach to the initial problem can identify the inconsistencies caused by the use of a particular numerical tool.

6.2. Flight test data

Open availability of flight data is completely lacking and poses a significant hurdle to scientists hoping to validate their numerical tools and ground based testing facilities. Some partnerships with private launch companies have led to the publishing of validation results, however these are all normalised to some unknown reference conditions which severely limits the usefulness to the research community [158,159]. It is however understandable that private launch companies keep the data to preserve any competitive advantage. From the perspective of the research community, costs of a flight test for scientific purposes is too high and is not feasible.

6.3. Applicability of heat flux scaling rules for retro-propulsion

The bulk of literature discusses thermal load predictions in the form of aerothermal databases, where simulations for specific trajectory points are run using at least two isothermal wall temperatures. These

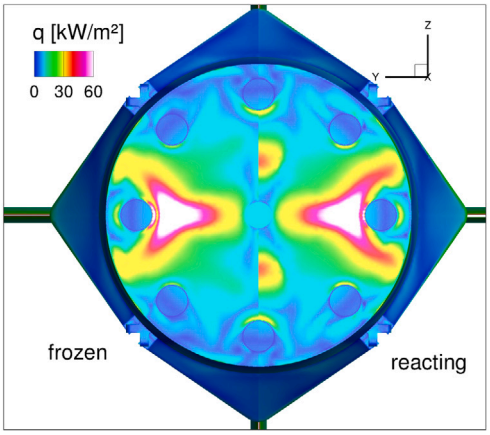

(a) Heating pattern comparison at the end of re-entry burn for the RETPRO vehicle at Mach 5.3, showing baseplate

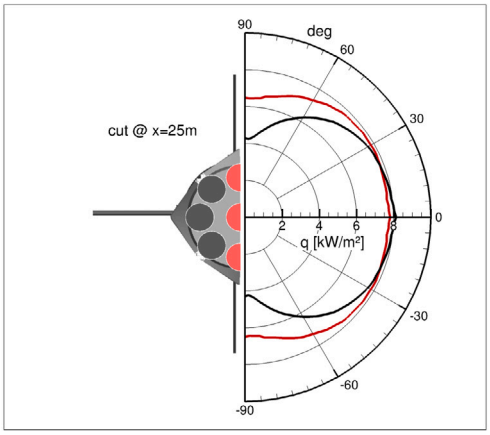

(b) Heating pattern comparison at the end of re-entry burn for the RETPRO vehicle at Mach 5.3, showing axial cut

Fig. 47. Heating pattern comparisons at the end of re-entry burn for the RETPRO vehicle at Mach 5.3 [45].

wall temperatures are chosen such that they cover the range of expected values for the entirety of the flight. This allows the use of fast response surrogate models with heat flux interpolation algorithms which are entirely independent of the material used for vehicle construction and their corresponding thicknesses or thermal properties [24,26,39,48,52,60,71,106,109,160,161]. This allows different structural models to be used to determine the wall temperature evolution through a flight. In addition, the use of different materials can be investigated using the generated database, provided that the wall temperature range of the database is not exceeded. In this case, supplementary simulations are required to allow interpolation to be completed. The use of aerothermal databases is in contrast to the method of using a heat transfer coefficient, which scales heat flux by considering a fixed isothermal wall temperature and the adiabatic wall temperature. This is because for complicated geometries which contain forward or backward facing steps, or flight conditions which make the vehicle susceptible to highly separated flows, such as high altitude retro-propulsion burns, the heat transfer coefficient appears to introduce errors dependent on the isothermal wall temperature selected [162]. Fig. 48 highlights the effective functioning of the heat coefficient in forward flight, where all tested wall temperatures collapse into one line. This is compared with the retro-propulsion case where a spread of 17% was observed between the lines. It is also key to observe the breakdown of the heat coefficient during forward flight in the base area (no active plume), further cementing the hypothesis of separated flows being the culprit for the issues observed in the retro-propulsion case.

One major drawback of the aerothermal database approach is that is relies on a significant number of computations to cover the trajectory adequately. The variety of spacecraft configurations and conditions experienced, such as changes in velocity, AoA, vehicle layout (fins unfolded or deflected, landing legs deployed etc.), engine conditions as well as altitude can significantly influence thermal loading. The nature of each of these conditions creating a unique aerothermal environment demands an increased number of computations to fulfil the needs of the aerothermal database, especially considering the two different wall temperature computations for each point to satisfy the minimum requirement for interpolation algorithms to function. Future work in this area would benefit greatly from new methods which allow strong predictions of aerothermal loads throughout the mission with a reduced number of computations or, through the development of lower order methods which are capable of predicting heat loads during retro-propulsion maneouvres. At present, the use of 2D RANS computations to provide guidance on the scaling of heat flux for a 3D geometry has been shown to effectively reduce the number of 3D simulations required for an aerothermal database and hence, reduce the computational cost [52]. However, this has not been tested on geometries which are not axisymmetric and requires further investigation to determine the applicability in this area. Fig. 49 shows the tuning of existing empirical formulations based on Sutton-Graves and Chapman to feed improved interpolations between trajectory points. The tuning was based on selected CFD anchor points and appears to be a promising technique for improving the interpolation algorithms [162], however this has not been extensively tested and it is likely that exponents used are case specific.

6.4. Dynamic stability derivatives

To date, only the aerodynamic characteristics of static configurations have been investigated. The study of vehicle dynamic motion, such as influence of pitch, yaw and roll rates on changes in the plume structure or the investigation of possible coupling effects between the vehicle and plume during these conditions may be of interest. To date, the determination of damping derivatives are limited to phases without active retro-propulsion [53] through the use of programs such as missile DATCOM [163]. This tool has a proven track record in allowing quick analysis of the aerodynamic characteristics of slender bodies and the design of key parameters such as fuselage diameter or fin size. However, re-usable launchers are often subjected to a wide Mach and AoA range, as well as various flight configurations, which highlights the limited applicability range of these low fidelity tools, making them insufficient for reusable VTVL launchers. Therefore, CFD methods, such as URANS, or wind tunnel tests are required for understanding the dynamic behaviour of the vehicle and any coupling effects that may be present.

6.5. Influence of plume radiation/characterisation of radiation

All CFD results to date look at convective heat fluxes, paying no attention to the possible effects of soot radiation. During ascent, the potential radiative heat flux from soot will be confined to the base area of the rocket, while during powered descent, the vehicle flies through its own exhaust and the effects of radiative heating may be noticed well upstream of the nozzles. The move to methane for future launchers will potentially limit this effect due to reduced soot production compared to kerosene fuelled rockets, where investigations have already shown that radiation can contribute significantly to the total heat flux [164,165]. Some investigations on subscale models suggest that the contribution to total heat flux at the wall of a methane engine is in the region of 10% [166], however soot production in full scale launcher engines still needs to be quantified.

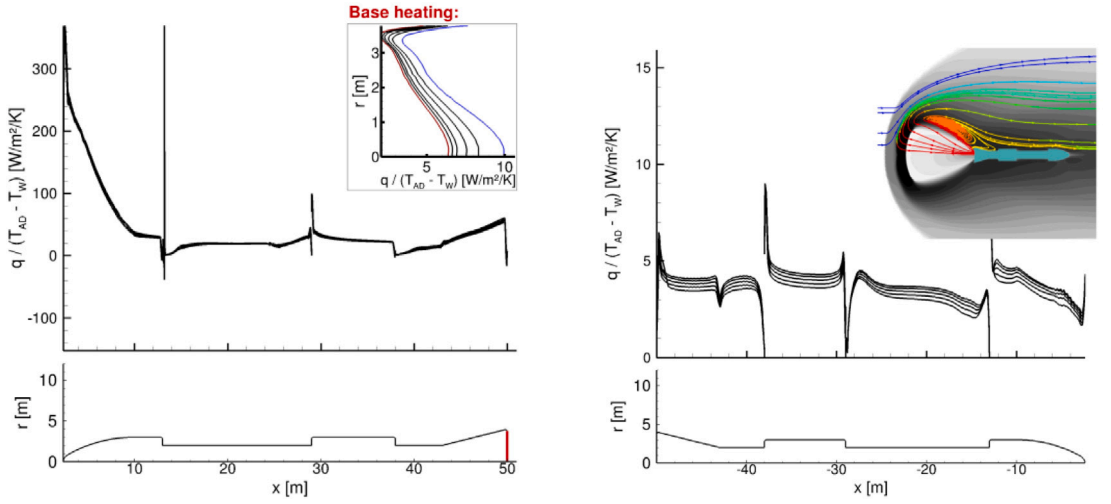

(a) Heat coefficient for forward flight based on multiple wall temperatures

(b) Heat coefficient for retro propulsion manoeuvre based on multiple wall temperatures

Fig. 48. Illustration of well functioning heat coefficient for forward flight compared with introduced error associated with retro-propulsion case [162].

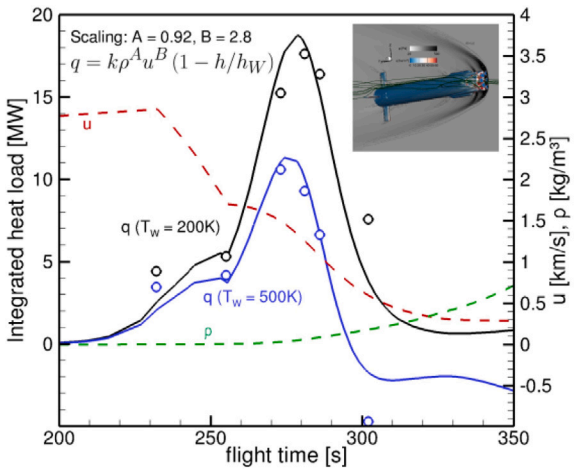

Fig. 49. Density–velocity scaling for the ENTRAIN-VL descent flight [162].

7. Conclusion

The use of retro-propulsion in earth based rocket systems is a new concept in the well established field of orbital class launcher design. It introduces a range of challenges for the prediction of aerodynamic and aerothermal characteristics of the vehicle, including the need to consider complex chemistry in the plume, as well as the highly unstable and fluctuating flow field which has been observed both experimentally and numerically. As of now, the only operational re-usable launcher is the SpaceX Falcon 9, which has been used as a benchmark for future launcher design within the realms of industry and research. While the next generation of vehicles is currently under development by a range of established players in the launcher scene, many of the design features seen on Falcon 9, such as retractable landing legs and deployable control surfaces, are being retained. A movement from kerosene to the cleaner burning methane fuel is also underway, which is anticipated to reduce refurbishment costs of the engines, as well as create a reduction in soot emission. The latter is expected to reduce radiative heat loads on the vehicle, but there is little literature on this topic and needs to be quantified in the future.

At present, the lack in availability of flight data means that the most effective way to generate aerodynamic and aerothermal databases, which are required to effectively model the flight and structural heating response, are limited to ground based testing and computational fluid dynamics. Unfortunately, historical tools which make use of fast, low fidelity methods allowing the exploration of a large design space, have been shown to lack the prediction capabilities for such a complex task. This is largely due to the requirement of accurate plume shape estimation, as well as phenomena such as plume-plume and plume-structure interactions.

Numerical datasets, which are largely limited to steady-state simulations, use mathematical models to estimate key phenomena associated with turbulence and chemistry. On the other hand, experimental facilities are able to provide uncertainties in the measurements taken, but are unable to provide results for a full scale configuration from an aerothermal and aerodynamic perspective. As a result, the shortcomings of both numerical and experimental data are addressed through a combined approach, where complementary analysis is conducted allowing uncertainties to be evaluated. This appears to be the most effective way to generate data for vehicle design until flight test data is available.

Credit authorship contribution statement

Tamas Bykerk: Writing – review & editing, Writing – original draft.
Sebastian Karl: Writing – review & editing, Writing – original draft.
Mariasole Laureti: Writing – review & editing, Writing – original draft.
Moritz Ertl: Writing – review & editing, Writing – original draft.
Tobias Ecker: Writing – review & editing, Writing – original draft.

Declaration of competing interest

The authors declare that they have no known competing financial interests or personal relationships that could have appeared to influence the work reported in this paper.

Data availability

No data was used for the research described in the article.

References

[1] A.M. Korzun, J.R. Cruz, R.D. Braun, A survey of supersonic retropropulsion technology for mars entry, descent, and landing, in: 2008 IEEE Aerospace Conference, 2008, pp. 1–15.

[2] Space X falcon 9, 2024, https://www.spacex.com/vehicles/falcon-9/. (Accessed 05 March 2024).

[3] E.S. Love, The effects of a small jet of air exhausting from the nose of a body of revolution in supersonic flow, 1952, https://api.semanticscholar.org/CorpusID:118813807.

[4] D.J. Romeo, J.R. Sterrett, L.R. Center., U. States., Exploratory Investigation of the Effect of a Forward-Facing Jet on the Bow Shock of a Blunt Body in a Mach Number 6 Free Stream, National Aeronautics and Space Administration, Washington, D.C., 1963, Includes bibliographical references (p. 13)., 45 p. http://hdl.handle.net/2027/uiug.30112106689513.

[5] P.J. Finley, The flow of a jet from a body opposing a supersonic free stream, J. Fluid Mech. 26 (2) (1966) 337–368.

[6] E.A. Barber, An experimental investigation of stagnation- point injection, J. Spacecr. Rockets 2 (5) (1965) 770–774, http://dx.doi.org/10.2514/3.28277, eprint: https://doi.org/10.2514/3.28277.

[7] L.O. Hayman, R.W. McDearmon, Jet effects on cylindrical afterbodies housing sonic and supersonic nozzles which exhaust against a supersonic stream at angles of attack from 90 degrees to 180 degrees, 1962, https://api.semanticscholar.org/CorpusID:118973647.

[8] V.L. Peterson, R.L. McKenzie, Effects of Simulated Retrorockets on the Aerodynamic Characteristics of a Body of Revolution at Mach Numbers from 0.25 to 1.90, National Aeronautics and Space Administration: [For sale by the Office of Technical Services, Dept. of Commerce, Washington, D.C., 1962, Includes bibliographical references., 45 p. http://hdl.handle.net/2027/uiug.30112106637595.

[9] R.J. McGhee, Effects of a Retro Nozzle Located at the Apex of a 140 Degree Blunt Cone at Mach Numbers of 3.00, 4.50, and 6.00, Tech. Rep., NASA, NASA TN D-6002, 1971.

[10] P. Jarvinen, R. Adams, Aerodynamic Characteristics of Large Angle Cones with Retrorockets, Tech. Rep., NASA, 1970.

[11] P.O. Jarvinen, J.A.F. Hill, Penetration of retrorocket exhausts into subsonic counterflows, J. Spacecr. Rockets 10 (1) (1973) 85–86, http://dx.doi.org/10.2514/3.27737, eprint: https://doi.org/10.2514/3.27737.

[12] R.D. Braun, R.M. Manning, Mars exploration entry, descent, and landing challenges, J. Spacecr. Rockets 44 (2) (2007) 310–323, http://dx.doi.org/10.2514/1.25116, eprint: https://doi.org/10.2514/1.25116.

[13] T. Polsgrove, et al., 2018 AIAA SPACE and astronautics forum and exposition. eprint: https://arc.aiaa.org/doi/abs/10.2514/6.2018-5192. https://arc.aiaa.org/doi/abs/10.2514/6.2018-5192.

[14] K.T. Edquist, Status of mars retropropulsion testing in the langley unitary plan wind tunnel, in: AIAA SCITECH 2022 Forum At: San Diego, USA, 2022, https://arc.aiaa.org/doi/abs/10.2514/6.2022-0911.

[15] K.T. Edquist, Testing of mars retropropulsion concepts in the langley unitary plan wind tunnel, in: AIAA Aviation and Aeronautics Forum and Exposition (2021 AIAA AVIATION Forum) At: Washington DC, USA, 2021.

[16] G. Nastac, et al., Computational investigation of the effect of chemistry on mars supersonic retropropulsion environments, in: AIAA SCITECH 2022 Forum At: Orlando, USA, 2022, https://arc.aiaa.org/doi/abs/10.2514/6.2022-2299.

[17] R.D. Braun, B. Sforzo, C. Campbell, AIAA SPACE and astronautics forum and exposition. eprint: https://arc.aiaa.org/doi/abs/10.2514/6.2017-5292. https://arc.aiaa.org/doi/abs/10.2514/6.2017-5292.

[18] M. Sippel, C. Manfletti, H. Burkhardt, Long-term/strategic scenario for reusable booster stages, Acta Astronaut. (ISSN: 0094-5765) 58 (4) (2006) 209–221, https://www.sciencedirect.com/science/article/pii/S0094576505003061.

[19] G. Woodcock, AIAA SPACE 2008 conference & exposition. eprint: https://arc.aiaa.org/doi/abs/10.2514/6.2008-7727. https://arc.aiaa.org/doi/abs/10.2514/6.2008-7727.

[20] E. Webb, D. Cundy, 5th international aerospace planes and hypersonics technologies conference. eprint: https://arc.aiaa.org/doi/abs/10.2514/6.1993-5008. https://arc.aiaa.org/doi/abs/10.2514/6.1993-5008.

[21] D. Preller, M.K. Smart, 20th AIAA international space planes and hypersonic systems and technologies conference. eprint: https://arc.aiaa.org/doi/abs/10.2514/6.2015-3586. https://arc.aiaa.org/doi/abs/10.2514/6.2015-3586.

[22] S. Stappert, et al., European next reusable ariane (ENTRAIN) : A multidisciplinary study on a VTVL and a VTHL booster stage, 2019, https://api.semanticscholar.org/CorpusID:210903590.

[23] S. Stappert, J. Wilken, M. Sippel, 2018 AIAA SPACE and astronautics forum and exposition. eprint: https://arc.aiaa.org/doi/abs/10.2514/6.2018-5239. https://arc.aiaa.org/doi/abs/10.2514/6.2018-5239.

[24] T. Ecker, S. Karl, E. Dumont, S. Stappert, D. Krause, Numerical study on the thermal loads during a supersonic rocket retropropulsion maneuver, J. Spacecr. Rockets 57 (1) (2020) 131–146, http://dx.doi.org/10.2514/1.A34486.

[25] J. Vos, et al., Aerodynamic investigations of a vertical landing launcher configuration by means of computational fluid dynamics and wind tunnel tests, in: AIAA Aviation 2022 Forum. AIAA SciTech Forum At: San Diego, USA, 2022.

[26] M. Laureti, S. Karl, A. Marwege, A. Gülhan, Aerothermal databases and CFD based load predictions, in: 2nd International Conference on Flight Vehicles, Aerothermodynamics and Re-Entry Missions Engineering At: Heilbronn, Germany, 2022.

[27] A. Marwege, et al., Key technologies for retro propulsive vertical descent and landing – RETALT – An overview, in: 2nd International Conference on Flight Vehicles, Aerothermodynamics and Re-Entry Missions Engineering At: Heilbronn, Germany, 2022.

[28] A. Marwege, et al., Aerodynamic phenomena of retro propulsion descent and landing configurations, in: 2nd International Conference on Flight Vehicles, Aerothermodynamics and Re-Entry Missions Engineering At: Heilbronn, Germany, 2022.

[29] A. Marwege, et al., RETALT: review of technologies and overview of design changes, CEAS Space J. (2022) http://dx.doi.org/10.1007/s12567-022-00458-9.

[30] A. Marwege, et al., Retro propulsion assisted landing technologies (RETALT): Current status and outlook of the EU fanded project on reusable launch vehicles, in: 70th International Astronautical Congress: Washington DC, USA, 2019.

[31] A. Marwege, et al., Wind tunnel experiments of interstage segments used for aerodynamic control of retro-propulsion assisted landing vehicles, CEAS Space J. (2022) http://dx.doi.org/10.1007/s12567-022-00425-4.

[32] D. Charbonnier, J. Vos, A. Marwege, C. Hantz, Computational fluid dynamics investigations of aerodynamic control surfaces of a vertical landing configuration, CEAS Space J. (2022) http://dx.doi.org/10.1007/s12567-022-00431-6.

[33] J. Vos, D. Charbonnier, A. Marwege, C. Hantz, A. Gülhan, CFD simulations and wind tunnel experiments for re-usable launch vehicles, in: 2nd International Conference on Flight Vehicles, Aerothermodynamics and Re-Entry Missions Engineering At: Heilbronn, Germany, 2022.

[34] A. Marwege, D. Kirchheck, J. Klevanski, A. Gülhan, Hypersonic retro-propulsion for reusable launch vehicles tested in the H2K wind tunnel, CEAS Space J. (2022) http://dx.doi.org/10.1007/s12567-022-00457-w.

[35] A. Marwege, A. Gülhan, Aerodynamic characteristics of the retro propulsion landing burn of vertically landing launchers, Exp. Fluids (2023) http://dx.doi.org/10.21203/rs.3.rs-3415270/v1.

[36] A. Marwege, A. Gülhan, Unsteady aerodynamics of the retropropulsion reentry burn of vertically landing launchers, J. Spacecr. Rockets 60 (6) (2023) 1939–1953, http://dx.doi.org/10.2514/1.A35647.

[37] A. Marwege, et al., Key technologies for retro propulsive vertical descent and landing - RETALT - An overview, in: 2nd International Conference on Flight Vehicles, Aerothermodynamics and Re-Entry Missions and Engineering (FAR), Heilbronn, Germany, 2022, http://dx.doi.org/10.5281/zenodo.6783915.

[38] A. Marwege, et al., RETALT1 – Aerodynamic Database 2.0, Zenodo, 2022, http://dx.doi.org/10.5281/zenodo.7027367.

[39] M. Laureti, S. Karl, Aerothermal databases and load predictions for Retro Propulsion-Assisted Launch Vehicles (RETALT), CEAS Space J. (2022) http://dx.doi.org/10.1007/s12567-021-00413-0.

[40] D. Kirchheck, et al., Validation of wind tunnel test and CFD techniques for retro-propulsion (RETPRO): Overview on a project within the future launchers preparatory programme (FLPP), in: 2nd International Conference on Flight Vehicles, Aerothermodynamics and Re-Entry Missions Engineering At: Monopoli, Italy, 2019.

[41] D. Kirchheck, A. Marwege, J. Klevanski, A. Gülhan, Hypersonic retrograde propulsion experiments - A basis for validation of CFD within RETPRO, in: 9th European Conference for Aeronautics and Space Sciences (EUCASS) At: Lille, France, 2022.

[42] T. Bykerk, D. Kirchheck, S. Karl, Reconstruction of wind tunnel tests using CFD for a reusable first stage during rocket retro-propulsion, in: 9th European Conference for Aeronautics and Space Sciences (EUCASS) At: Lille, France, 2022.

[43] T. Bykerk, S. Karl, Preparatory CFD studies for subsonic analyses of a reusable first stage launcher during landing within the RETPRO project, in: 10th EUCASS – 9th CEAS Conference 2023. 10th EUCASS – 9th CEAS Conference 2023 At: Lausanne, Switzerland, 2023.

[44] T. Bykerk, D. Kirchheck, S. Karl, S. Fechter, Condensation modelling of expanding cold gas jets during hypersonic retro-propulsion manoeuvres within the RETPRO project, in: Proceedings of the Australasian Fluid Mechanics Conference At: Sydney, Australia, 2022.

[45] M. Laureti, S. Karl, T. Bykerk, D. Kirchheck, Aerothermal analysis of the RETPRO flight configuration, in: 9th Space Propulsion Conference 2024, 2024.

[46] A. Marwege, D. Kirchheck, A. Gülhan, First hot combustion subsonic retro propulsion tests in the vertical free jet facility cologne (VMK), in: 3rd International Conference on High-Speed Vehicle Science & Technology HISST 2024, 2024.

[47] FROG project: small demonstrator for big ambitions in RLV European objectives. Status quo and results.

[48] M. Ertl, T. Ecker, J. Klevanski, E. Dumont, S. Krummen, Aerothermal analysis of plume interaction with deployed landing legs of the CALLISTO vehicle, in: 9th European Conference for Aeronautics and Space Sciences (EUCASS) At: Lille, France, 2022.

[49] E. Dumont, et al., CALLISTO: Towards reusability of a rocket stage: Current status, J. Evol. Space Activities 1 (2023) 75.

[50] S. Krummen, et al., Applying Bayesian inference to estimate uncertainties in the aerodynamic database of CALLISTO, in: IEEE Aerospace Conference, 2023, https://elib.dlr.de/189084/.

[51] E. Dumont, et al., CALLISTO: A prototype paving the way for reusable launch vehicles in Europe and Japan, in: 73rd International Astronautical Congress (IAC) At: Paris, France, 2022.

[52] T. Ecker, M. Ertl, J. Klevanski, S. Krummen, E. Dumont, Aerothermal characterization of the CALLISTO vehicle during descent, in: 9th European Conference for Aeronautics and Space Sciences (EUCASS) At: Lille, France, 2022.

[53] J. Klevanski, et al., Progress in aerodynamic studies for CALLISTO - reusable VTVL launcher first stage demonstrator, in: 9th European Conference for Aeronautics and Space Sciences (EUCASS) At: Lille, France, 2022.

[54] E. Dumont, et al., CALLISTO: towards reusability of a rocket stage: current status, in: 33rd ISTS Conference At: Beppu, Japan, 2022.

[55] E. Dumont, et al., CALLISTO - reusable VTVL launcher first stage demonstrator, in: Space Propulsion Conference At: Seville, Spain, 2018.

[56] J. Klevanski, et al., Aerodynamic studies in preparation for CALLISTO - reusable VTVL launcher first stage demonstrator, in: 69th International Astronautical Congress (IAC) At: Bremen, Germany, 2018.

[57] E. Dumont, et al., CALLISTO: a demonstrator for reusable launcher key technologies, in: 32nd ISTS At: Fukui, Japan, 2019.

[58] A. Marwege, et al., First wind tunnel data of CALLISTO - Reusable VTVL launcher first stage demonstrator, in: EUCASS 2019 At: Madrid, Spain, 2019.

[59] S. Guédron, et al., CALLISTO DEMONSTRATOR: Focus on system aspects, in: 71st International Astronautical Congress At: Online, 2020.

[60] M. Ertl, T. Ecker, Aerodynamic and aerothermal comparison between the CAL1C and CAL1D geometries for the CALLISTO vehicle, in: 10th EUCASS – 9th CEAS Conference 2023. 10th EUCASS – 9th CEAS Conference 2023 At: Lausanne, Switzerland, 2023.

[61] J. Riehmer, A. Marwege, J. Klevanski, A. Gülhan, E. Dumont, Subsonic and supersonic ground experiments for the CALLISTO VTVL launcher demonstrator, in: 2nd International Conference on Flight Vehicles, Aerothermodynamics and Re-Entry Missions Engineering At: Monopoli, Italy, 2019.

[62] A. Marwege, J. Riehmer, J. Klevanski, A. Gülhan, E. Dumont, Wind tunnel investigations in CALLISTO - Reusable VTVL launcher first stage demonstrator, in: 70th International Astronautical Congress: Washington DC, USA, 2019.

[63] M. Ertl, Y. Feldner, T. Ecker, Numerical investigation of ground heat fluxes from supersonic jet impingement during vertical landing of a reusable first stage demonstrator, in: 2nd International Conference on High-Speed Vehicle Science & Technology HISST 2022, CEAS, 2022, pp. 1–13, https://elib.dlr.de/187883/.

[64] E. Dumont, et al., CALLISTO: A demonstrator for reusable launcher key technologies, Trans. JSASS Aerospace Tech. Jpn 19 (1) (2021) 106–115.

[65] T. Ecker, M. Ertl, J. Klevanski, S. Krummen, E. Dumont, Aerothermal characterization of the CALLISTO vehicle during descent, CEAS Space J. (ISSN: 1868-2510) (2024) http://dx.doi.org/10.1007/s12567-024-00561-z.

[66] Technology acceleration process for the THEMIS low cost and reusable prototype.

[67] Salto project, 2024, https://salto-project.eu/. (Accessed 14 June 2024).

[68] Rfz-Model, Rfz-model/RFZ_data: Post HiSST 2024 (post_hisst_2024), 2023, http://dx.doi.org/10.5281/zenodo.11045747.

[69] T. Bykerk, A standard model for the investigation of aerodynamic and aerothermal loads on a re-usable launch vehicle, in: 10th EUCASS – 9th CEAS Conference 2023. 10th EUCASS – 9th CEAS Conference 2023 At: Lausanne, Switzerland, 2023.

[70] Spacex aims to launch 144 missions next year, 2024, https://www.space.com/spacex-launch-144-missions-2024. (Accessed 05 March 2024).

[71] S. Karl, T. Bykerk, Sustainable space technologies – Strategies towards a predictive aerothermal design of re-usable space transportation systems, Rev. Sci. Instrum. (2024) tbc.

[72] T.D. Wood, H.S. Kanner, D.M. Freeland, D.T. Olson, Solid rocket booster (SRB) flight system integration at its best, 2011, https://api.semanticscholar.org/CorpusID:106986393.

[73] How to bring a rocket back from space, 2024, https://www.rocketlabusa.com/updates/how-to-bring-a-rocket-back-from-space/. (Accessed 14 June 2024).

[74] G.D. Zaiacomo, G.B. Arnao, R. Bunt, D. Bonetti, Mission engineering for the retalt vtvl launcher, CEAS Space Journal (ISSN: 1868-2510) 14 (3) (2022) 533–549, https://doi.org/10.1007/s12567-021-00415-y.

[75] G. Chapman, Theoretical Laminar Convective Heat Transfer and Boundary Layer Characteristics on Cones at Speeds to 24 km/s, NASA Technical Note D-2463, NASA, 1964.

[76] J. Bradford, B. St. Germain, K. Feld, Optimization of a reusable rocket-powered, VTVL launch system: A case study of the falcon 9-R, 2014, https://docplayer.net/25483752-Optimization-of-a-reusable-rocket-powered-vtvl-launch-system-a-case-study-of-the-falcon-9-r.html.

[77] J. Desmariaux, T. Lienart, N. Perbet, S. Ishimoto, Y. Saito, H. Adachi, Y. Minami, L. Witte, A. Schneider, J. Windelberg, S. Eichel, Overview of callisto vehicle development status, 10th EUCASS – 9th CEAS Conference 2023. Conference 2023 At: Lausanne, Switzerland (2023) http://dx.doi.org/10.13009/EUCASS2023-998.

[78] E.C. Holleman, Summary of high-altitude and entry flight control experience with the x-15 airplane, in: NASA Technical Note, 1966, National Aeronautics and Space Administration, Washington, D.C., 1966-04.

[79] E. Schuelein, D. Guyot, Novel high-performance grid fins for missile control at high speeds: Preliminary numerical and experimental investigations, 2006, https://api.semanticscholar.org/CorpusID:53966459.

[80] K.S. Orthner, Aerodynamic analysis of lattice grid fins in transonic flow, 2012, https://api.semanticscholar.org/CorpusID:107385347.

[81] F. Hiroshima, K. Tatsumi, Grid pattern effects on aerodynamic characteristics of grid fins, in: 24th International Congress of the Aeronautical Sciences, Mitsubishi Electric Corporation, Kamakura Works, Kanagawa, Japan.

[82] https://arc.aiaa.org/doi/abs/10.2514/6.2001-256 E. Fournier, Wind tunnel investigation of grid fin and conventional planar control surfaces, in: 39th Aerospace Sciences Meeting and Exhibit, http://dx.doi.org/10.2514/6.2001-256, arXiv:https://arc.aiaa.org/doi/pdf/10.2514/6.2001-256.

[83] S. Munawar, Analysis of grid fins as efficient control surface in comparison to conventional planar fins, in: 27th International Congress of the Aeronautical Sciences, 2010.

[84] Starship, 2024, https://www.spacex.com/vehicles/starship/. (Accessed 07 June 2024).

[85] Neutron, 2024, https://www.rocketlabusa.com/launch/neutron/. (Accessed 14 June 2024).

[86] New glenn, 2024, https://www.blueorigin.com/new-glenn. (Accessed 14 June 2024).

[87] D.F. Fisher, D.G. Murri, Forebody Aerodynamics of the F-18 High Alpha Research Vehicle with Actuated Forebody Strakes, Tech. Rep., NASA Dryden Flight Research Center and NASA Langley Research Center, MS 2228, P.O. Box 273, Edwards, CA 93523-0273, USA and MS 153, Hampton, VA 23681-2199, USA.

[88] H. Taguchi, et al., Systems analysis on hypersonic airplanes using pre-cooled turbojet engine, in: 17th AIAA International Space Planes and Hypersonic Systems and Technologies Conference, San Francisco, California, 2011.

[89] T. Bykerk, D. Verstraete, J. Steelant, Low speed longitudinal aerodynamic, static stability and performance analysis of a hypersonic waverider, Aerosp. Sci. Technol. (ISSN: 1270-9638) 96 (2020) 105531, https://www.sciencedirect.com/science/article/pii/S1270963819323387.

[90] T. Bykerk, D. Verstraete, J. Steelant, Low speed lateral-directional aerodynamic and static stability analysis of a hypersonic waverider, Aerosp. Sci. Technol. 98 (2020) https://www.scopus.com/inward/record.uri?eid=2-s2.0-85078450517&doi=10.1016%2fj.ast.2020.105709&partnerID=40&md5=98da889484e1dc0bd2aa858a89b9fcb1, Cited by: 25.

[91] H. Burkhardt, M. Sippel, A. Herbertz, J. Klevanski, Kerosene vs. Methane: A propellant tradeoff for reusable liquid booster stages, J. Spacecr. Rockets 41 (5) (2004) 762–769, http://dx.doi.org/10.2514/1.2672.

[92] P. Pempie, T. Froehlich, H. Vernin, LOX/methane and LOX/kerosene high thrust engine trade-off, in: 37th Joint Propulsion Conference and Exhibit, eprint: https://arc.aiaa.org/doi/abs/10.2514/6.2001-3542, https://arc.aiaa.org/doi/abs/10.2514/6.2001-3542.

[93] K. Liang, B. Yang, Z. Zhang, Investigation of heat transfer and coking characteristics of hydrocarbon fuels, J. Propuls. Power 14 (5) (1998) 789–796, http://dx.doi.org/10.2514/2.5342.

[94] A. Goetz, C. Maeding, L. Brummel, D. Haeseler, Application of non-toxic propellants for future launch vehicles, in: 37th Joint Propulsion Conference and Exhibit, eprint: https://arc.aiaa.org/doi/abs/10.2514/6.2001-3546, https://arc.aiaa.org/doi/abs/10.2514/6.2001-3546.

[95] I. Klepikov, B. Katorgin, V. Chvanov, The new generation of rocket engines, operating by ecologically safe propellant "liquid oxygen and liquefied natural gas(methane)", Acta Astronaut. (ISSN: 0094-5765) 41 (4) (1997) 209–217, eprint: https://www.sciencedirect.com/science/article/pii/S0094576598000769.

[96] G. Scarlatella, M. Tajmar, C. Bach, Advanced nozzle concepts in retro-propulsion applications for reusable launch vehicle recovery: a case study, in: 72nd International Astronautical Congress (IAC) At: Dubai, UAE, 2021.

[97] G. Scarlatella, et al., Cold-gas experiments on advanced nozzles in subsonic counter-flows, in: 10th EUCASS – 9th CEAS Conference 2023. 10th EUCASS – 9th CEAS Conference 2023 At: Lausanne, Switzerland, 2023.

[98] G. Scarlatella, et al., Design and development of a cold-flow test-bench for study of advanced nozzles in subsonic counter-flows, Aerotecnica Missili Spazio 101 (2022) 201–213.

[99] B.S. Venkatachari, M. Mullane, G. Cheng, C.-L. Chang, Numerical study of counterflowing jet effects on supersonic slender-body configurations, in: 33rd AIAA Applied Aerodynamics Conference, 2015, eprint: https://arc.aiaa.org/doi/abs/10.2514/6.2015-3010, https://arc.aiaa.org/doi/abs/10.2514/6.2015-3010.

[100] K. Gutsche, A. Marwege, A. Gülhan, Similarity and key parameters of retro-propulsion assisted deceleration in hypersonic wind tunnels, J. Spacecr. Rockets 58 (4) (2021) 984–996, http://dx.doi.org/10.2514/1.A34910.

[101] Feeding the beast: Super heavy's propellant distribution system, 2024, https://ringwatchers.com/article/booster-prop-distribution. (Accessed 07 June 2024).

[102] [4K] watch spacex starship FLIGHT 4 launch and reenter LIVE!, 2024, https://www.youtube.com/watch?v=8VESowgMbjA. (Accessed 07 June 2024).

[103] X. Wang, X. Xu, Q. Yang, Numerical analysis on thermal environment of reusable launch vehicle during supersonic retropropulsion, Int. J. Therm. Sci. (ISSN: 1290-0729) 198 (2024) 108857, https://www.sciencedirect.com/science/article/pii/S1290072923007184.

[104] P.V. Raje, K. Sinha, AIAA aviation 2019 forum, eprint: https://arc.aiaa.org/doi/abs/10.2514/6.2019-3322. https://arc.aiaa.org/doi/abs/10.2514/6.2019-3322,

[105] K. Deere, A. Elmlilgui, K.S. Abdol-Hamid, Usm3d simulations of saturn v plume induced flow separation, in: 49th AIAA Aerospace Sciences Meeting Including the New Horizons Forum and Aerospace Exposition, 2011, AIAA Paper 2011-1055, NF1676L-10816, NASA Langley Research Center, Hampton, VA, United States, January 4-7, 2011, Orlando, FL, American Institute of Aeronautics and Astronautics.

[106] F. Zilker, T. Ecker, E. Dumont, K. Hannemann, Aerothermal analysis of reusable first stage launcher during re-entry retro-propulsion, in: 18. STAB-Workshop At: GÖttingen, Germany, 2017.

[107] T. Bykerk, Reusable launchers: challenges for the prediction of aerodynamic characteristics and thermal loads, in: Australasian Fluid Mechanics Society: Conversations in Fluids 2024, 2024.

[108] S.F. Hoerner, Fluid dynamic drag: Practical information on aerodynamic drag and hydrodynamic resistance, 1965.

[109] T. Ecker, S. Karl, E. Dumont, S. Stappert, D. Krause, A numerical study on the thermal loads during a supersonic rocket retro-propulsion maneuver, in: 53rd AIAA/SAE/ASEE Joint Propulsion Conference At: Atlanta, USA, 2017.

[110] S. Karl, T. Bykerk, CFD Test Report for the Flight Configuration (D3-3), DLR Report, DLR, 2023.

[111] Y. Feldner, M. Ertl, T. Ecker, S. Karl, Numerical investigation of the effects of post-combustion due to fuel outflow in bleed engine cycles of a retro propulsion-assisted launch vehicle, in: 10th EUCASS – 9th CEAS Conference 2023. 10th EUCASS – 9th CEAS Conference 2023 At: Lausanne, Switzerland, 2023.

[112] K. Hannemann, J. Martinez Schramm, A. Wagner, G. Ponchio Camillo, The high enthalpy shock tunnel göttingen of the german aerospace center (dlr), Journal of Large-Scale Research Facilities (ISSN: 2364-091X) 4 (A133) (2018) 1–14, http://dx.doi.org/10.17815/jlsrf-4-168, https://doi.org/10.17815/jlsrf-4-168.

[113] S.A. Berry, et al., Supersonic Retropropulsion Experimental Results from the NASA Langley Unitary Plan Wind Tunnel, AIAA Paper 2011-13217, NASA Langley Research Center, 2011, https://ntrs.nasa.gov/api/citations/20110013217/downloads/20110013217.pdf.

[114] A.T. Hoang, N.J. Lawson, T. Bykerk, Design of a wind tunnel model for a reusable launch vehicle during its landing burn, in: ICAS 2024.

[115] https://arc.aiaa.org/doi/abs/10.2514/6.2013-27 B. Palaszewski, Entry, descent, and landing with propulsive deceleration: supersonic retropropulsion wind tunnel testing and shock phenomena, in: 51st AIAA Aerospace Sciences Meeting including the New Horizons Forum and Aerospace Exposition, http://dx.doi.org/10.2514/6.2013-27, arXiv:https://arc.aiaa.org/doi/pdf/10.2514/6.2013-27.

[116] K.A. Trumble, et al., Analysis of Navier-Stokes Codes Applied to Supersonic Retro-Propulsion Wind Tunnel Test, IEEE Aerospace Conference Proceedings, NASA Ames Research Center, 2011, http://dx.doi.org/10.1109/AERO.2011.5747241, https://ntrs.nasa.gov/api/citations/20110013217/downloads/20110013217.pdf.

[117] H. Olivier, S. Gu, Operation, Capabilities and Limitations of Existing Hypersonic Facilities, Tech. Rep., Shock Wave Laboratory, RWTH Aachen University, Germany, 2020.

[118] D. Liechty, S. Berry, T. Horvath, Shuttle Return to Flight Experimental Results: Protuberance Effects on Boundary Layer Transition, Technical Report NASA-TM-2006-214306, NASA, Langley Research Center, Hampton, VA, 2006.

[119] C.G. Miller, Experimental investigation of Gamma effects on heat transfer to a 0.006 scale shuttle orbiter at mach 6, in: AIAA/ASME 3rd Joint Thermophysics, Fluids, Plasma and Heat Transfer Conference, St. Louis, Missouri, 1982.

[120] A.B. Blair, Effect of Reynolds Number on the Aerodynamic Stability and Control of a 55 Degree Clipped-Delta-Wing Orbiter Configuration at Supersonic Mach Numbers, Technical Report NASA-TM-X-3376, NASA, Washington, DC, 1976.

[121] H. Rosemann, The cryogenic ludwieg-tube at göttingen, in: Special Course on Advances in Cryogenic Wind Tunnel Technology, AGARD-R-812, DLR, Cologne, Germany, 1996.

[122] A.M. Korzun, L.A. Cassel, Scaling and similitude in single nozzle supersonic retropropulsion aerodynamics interference, in: AIAA Scitech 2020 Forum.

[123] A. Marwege, Aerodynamic analyses of retro-propulsion assisted descent and landing of launcher configurations, in: PhD Thesis, RWTH Aachen University, 2024, https://publications.rwth-aachen.de/record/989402.

[124] A.M. Korzun, L.A. Cassel, Scaling and similitude in single nozzle supersonic retropropulsion aerodynamics interference, in: AIAA Scitech 2020 Forum At: Orlando, USA, 2022, https://arc.aiaa.org/doi/abs/10.2514/6.2020-0039.

[125] T.Q. Huang, G. He, Q. Wang, Calculation of aerodynamic characteristics of hypersonic vehicles based on the surface element method, Adv. Aerosp. Sci. Technol. 7 (2022) 112–122.

[126] W.H. Heybey, Newtonian Aerodynamics for general Body Shapes with Several Applications, Tech. Rep. NASA Technical Memorandum, TM X-53391, George C. Marshall Space Flight Center, 1966.

[127] A.J. Eggers, R.C. Savin, C.A. Syvertson, The generalized shock-expansion method and its application to bodies traveling at high supersonic air speeds, J. Aeronaut. Sci. 22 (4) (1955) 231–238.

[128] S.A. Whitmore, Real gas extensions to tangent-wedge and tangent-cone analysis methods, AIAA J. 45 (8) (2007) 2024–2032.

[129] M.C. Adams, W.R. Sears, Slender-body theory-review and extension, J. Aeronaut. Sci. 20 (2) (1953) 85–98.

[130] J.D. Anderson, Hypersonic and High-Temperature Gas Dynamics, American Institute of Aeronautics and Astronautics, Inc, 2019.

[131] C.E. Cordell, R.D. Braun, An analytical approach to modeling supersonic retropropulsion flow field components, in: AIAA Atmospheric Flight Mechanics Conference, eprint: https://arc.aiaa.org/doi/abs/10.2514/6.2014-1093, https://arc.aiaa.org/doi/abs/10.2514/6.2014-1093.

[132] A.M. Korzun, R.D. Braun, Conceptual modeling of supersonic retropropulsion flow interactions and relationships to system performance, J. Spacecr. Rockets 50 (6) (2013) 1121–1133, http://dx.doi.org/10.2514/1.A32464.

[133] A.L. Knutson, J.S. Thome, G.V. Candler, Numerical simulation of instabilities in the boundary-layer transition experiment flowfield, J. Spacecr. Rockets 58 (1) (2021) 90–99.

[134] R.W. MacCormack, Carbuncle computational fluid dynamics problem for blunt-body flows, J. Aerosp. Inf. Syst. 10 (5) (2013) 229–239.

[135] G.V. Candler, P.K. Subbareddy, I. Nompelis, CFD Methods for Hypersonic Flows and Aerothermodynamics, in: Hypersonic Nonequilibrium Flows: Fundamentals and Recent Advances, 2015, pp. 203–237.

[136] F.G. Schmitt, About Boussinesq's turbulent viscosity hypothesis: historical remarks and a direct evaluation of its validity, C. R. Méc. (ISSN: 1631-0721) 335 (9) (2007) 617–627, https://www.sciencedirect.com/science/article/pii/S1631072107001386, Joseph Boussinesq, a Scientist of bygone days and present times.

[137] F. Hamba, Nonlocal analysis of the Reynolds stress in turbulent shear flow, Phys. Fluids 17 (11) (2005) 115102.

[138] R.-D. Cécora, R. Radespiel, B. Eisfeld, A. Probst, Differential Reynolds-stress modeling for aeronautics, AIAA J. 53 (3) (2015) 739–755.

[139] D.C. Wilcox, Turbulence Modeling for CFD, DCW Industires, Inc., 2006.

[140] S. Sarkar, The pressure–dilatation correlation in compressible flows, Phys. Fluids A (ISSN: 0899-8213) 4 (12) (1992) 2674–2682.

[141] O. Zeman, Dilatation dissipation: The concept and application in modeling compressible mixing layers, Phys. Fluids A (ISSN: 0899-8213) 2 (2) (1990) 178–188.

[142] M.F. Barone, W.L. Oberkampf, F.G. Blottner, Validation case study: Prediction of compressible turbulent mixing layer growth rate, AIAA J. 44 (7) (2006) 1488–1497.

[143] G.L. Brown, A. Roshko, On density effects and large structure in turbulent mixing layers, J. Fluid Mech. 64 (4) (1974) 775–816.

[144] P.J. Strykowski, D.L. Niccum, The influence of velocity and density ratio on the dynamics of spatially developing mixing layers, Phys. Fluids A 4 (4) (1992) 770–781.

[145] D. Davidenko, I. Gökalp, E. Dufour, P. Magre, AIAA/CIRA 13th International Space Planes and Hypersonics Systems and Technologies Conference, AIAA-Paper 2005-3237.

[146] J. Larsson, I. Bermejo-Moreno, S.K. Lele, Reynolds- and mach-number effects in canonical shock–turbulence interaction, J. Fluid Mech. 717 (2013) 293–321.

[147] K. Sinha, K. Mahesh, G.V. Candler, Modeling the effect of shock unsteadiness in shock/ turbulent boundary-layer interactions, AIAA J. 43 (3) (2005) 586–594.

[148] K. Brinckman, D. Kenzakowski, S. Dash, 43rd AIAA aerospace sciences meeting and exhibit, AIAA-Paper 2005-508.

[149] K.W. Brinckman, W.H. Calhoon, S.M. Dash, Scalar fluctuation modeling for high-speed aeropropulsive flows, AIAA J. 45 (5) (2007) 1036–1046.

[150] J.C. Oefelein, Mixing and combustion of cryogenic oxygen-hydrogen shear-coaxial jet flames at supercritical pressure, Combust. Sci. Technol. 178 (1–3) (2006) 229–252.

[151] S. Karl, M. Laureti, Deliverable D 3.7: Aerothermal Loads, Tech. Rep., DLR, 2020.

[152] M. Laureti, S. Karl, Retalt Report: D3.7 Aerothermal Loads, DLR Report, DLR, 2023.

[153] N. Zettervall, C. Fureby, E.J.K. Nilsson, Evaluation of chemical kinetic mechanisms for methane combustion: A review from a CFD perspective, Fuels (ISSN: 2673-3994) 2 (2) (2021) 210–240, https://www.mdpi.com/2673-3994/2/2/13.

[154] C.K. Westbrook, F.L. Dryer, Simplified reaction mechanisms for the oxidation of hydrocarbon fuels in flames, Combust. Sci. Technol. 27 (1–2) (1981) 31–43, http://dx.doi.org/10.1080/00102208108946970.

[155] P. Gerlinger, H. Möbus, D. Brüggemann, An implicit multigrid method for turbulent combustion, J. Comput. Phys. (ISSN: 0021-9991) 167 (2) (2001) 247–276, https://www.sciencedirect.com/science/article/pii/S0021999100966713.

[156] J.P. Slotnick, et al., CFD Vision 2030 Study: A Path to Revolutionary Computational Aerosciences, Tech. Rep. NASA/CR-2014-218178, NASA, 2014, https://ntrs.nasa.gov/api/citations/20160006942/downloads/20160006942.pdf.

[157] D. Saile, D. Kirchheck, A. Gülhan, D. Banuti, Design of a hot plume interaction facility at DLR cologne, in: 8th European Symposium on Aerothermodynamics for Space Vehicles: Lisbon, Portugal, 2015.

[158] K.T. Edquist, et al., Comparison of Navier-Stokes flow solvers to falcon 9 supersonic retropropulsion flight data, in: AIAA SPACE and Astronautics Forum and Exposition, 2017.
[159] T.J. Horvath, et al., Advancing supersonic retro-propulsion technology readiness: Infrared observations of the spacex falcon 9 first stage, in: AIAA SPACE and Astronautics Forum and Exposition, 2017, https://arc.aiaa.org/doi/abs/10.2514/6.2017-5294.
[160] T. Ecker, F. Zilker, E. Dumont, S. Karl, Hannemann, Aerothermal analysis of reusable launcher systems during retro-propulsion reentry and landing, in: Space Propulsion Conference At: Seville, Spain, 2018.
[161] M. Laureti, S. Karl, Aerothermal analysis of the RETALT2 SSTO vehicle, in: 10th EUCASS – 9th CEAS Conference 2023. 10th EUCASS – 9th CEAS Conference 2023 At: Lausanne, Switzerland, 2023.
[162] S. Karl, J. Wilken, L. Bussler, Aerothermal databases and heat-load prediction for re-usable launch vehicle configurations, in: HiSST, 2nd International Conference on High-Speed Vehicle Science and Technology, CEAS, 2022, pp. 1–14, https://elib.dlr.de/188605/.
[163] W.B. Blake, Missile DATCOM User's Manual - 1997 FORTRAN 90 Revision, Air Vehicles Directorate, Air Force Research Laboratory, Air Force Materiel Command, Wright Patterson Air Force Base, Ohio 45433-7562, 1998.
[164] J. Kim, Estimation and measurement of base heating on test launch vehicle, in: 8th European Conference for Aeronautics and Space Sciences, EUCASS, Korea Aerospace Research Institute, 2019.
[165] D. Byun, S.W. Baek, Numerical investigation of combustion with non-gray thermal radiation and soot formation effect in a liquid rocket engine, Int. J. Heat Mass Transfer (ISSN: 0017-9310) 50 (3) (2007) 412–422, https://www.sciencedirect.com/science/article/pii/S0017931006005606.
[166] F. Göbel, B. Kniesner, M. Frey, O. Knab, C. Mundt, Radiative heat transfer analysis in modern rocket combustion chambers, in: 5th European Conference for Aeronautics and Space Sciences, EUCASS, EUCASS association, Munich, Germany, 2013, https://elib.dlr.de/188605/1/hisst2020_karl.pdf.